Astronomy & Astrophysics

Deciphering the extreme X-ray variability of the nuclear transient eRASSt J045650.3−203750

A likely repeating partial tidal disruption event

Z. Liu[1], A. Malyali[1], M. Krumpe[2], D. Homan[2], A. J. Goodwin[3], I. Grotova[1], A. Kawka[3], A. Rau[1], A. Merloni[1], G. E. Anderson[3], J. C. A. Miller-Jones[3], A. G. Markowitz[4,5], S. Ciroi[6], F. Di Mille[7], M. Schramm[8], S. Tang[9], D. A. H. Buckley[10,11,12], M. Gromadzki[13], C. Jin[14,15], and J. Buchner[1]

[1] Max-Planck-Institut für extraterrestrische Physik, Gießenbachstraße 1, 85748 Garching, Germany
e-mail: liuzhu@mpe.mpg.de
[2] Leibniz-Institut für Astrophysik Potsdam, An der Sternwarte 16, 14482 Potsdam, Germany
[3] International Centre for Radio Astronomy Research, Curtin University, GPO Box U1987, Perth, WA 6845, Australia
[4] Nicolaus Copernicus Astronomical Center, Polish Academy of Sciences, ul. Bartycka 18, 00-716 Warszawa, Poland
[5] University of California, San Diego, Center for Astrophysics and Space Sciences, MC 0424, La Jolla, CA 92093-0424, USA
[6] Dipartimento di Fisica e Astronomia "G. Galilei", Università di Padova, Vicolo dell'Osservatorio 3, 35122 Padova, Italy
[7] Las Campanas Observatory, Carnegie Observatories, Colina El Pino, Casilla 601, La Serena, Chile
[8] Graduate school of Science and Engineering, Saitama Univ. 255 Shimo-Okubo, Sakura-ku, Saitama City, Saitama 338-8570, Japan
[9] Department of Physics, The University of Tokyo, 7-3-1 Hongo, Bunkyo-ku, Tokyo 113-0033, Japan
[10] South African Astronomical Observatory, PO Box 9, Observatory Road, Observatory 7935, Cape Town, South Africa
[11] Department of Astronomy, University of Cape Town, Private Bag X3, Rondebosch 7701, South Africa
[12] Department of Physics, University of the Free State, PO Box 339, Bloemfontein 9300, South Africa
[13] Astronomical Observatory, University of Warsaw, Al. Ujazdowskie 4, 00-478 Warszawa, Poland
[14] National Astronomical Observatories, Chinese Academy of Sciences, 20A Datun Road, Beijing 100101, PR China
[15] School of Astronomy and Space Sciences, University of Chinese Academy of Sciences, 19A Yuquan Road, Beijing 100049, PR China

ABSTRACT

Context. During its all-sky survey, the extended ROentgen Survey with an Imaging Telescope Array (eROSITA) on board the Spectrum-Roentgen-Gamma (SRG) observatory has uncovered a growing number of X-ray transients associated with the nuclei of quiescent galaxies. Benefitting from its large field of view and excellent sensitivity, the eROSITA window into time-domain X-ray astrophysics yields a valuable sample of X-ray selected nuclear transients. Multi-wavelength follow-up enables us to gain new insights into understanding the nature and emission mechanism of these phenomena.

Aims. We present the results of a detailed multi-wavelength analysis of an exceptional repeating X-ray nuclear transient, eRASSt J045650.3−203750 (hereafter J0456−20), uncovered by SRG/eROSITA in a quiescent galaxy at a redshift of $z \sim 0.077$. We aim to understand the radiation mechanism at different luminosity states of J0456−20, and provide further evidence that similar accretion processes are at work for black hole accretion systems at different black hole mass scales.

Methods. We describe our temporal analysis, which addressed both the long- and short-term variability of J0456−20. A detailed X-ray spectral analysis was performed to investigate the X-ray emission mechanism.

Results. Our main findings are that (1) J0456−20 cycles through four distinctive phases defined based on its X-ray variability: an X-ray rising phase leading to an X-ray plateau phase that lasts for abouttwo months. This is terminated by a rapid X-ray flux drop phase during which the X-ray flux can drop drastically by more than a factor of 100 within one week, followed by an X-ray faint state for about two months before the X-ray rising phase starts again. (2) The X-ray spectra are generally soft in the rising phase, with a photon index $\gtrsim 3.0$, and they become harder as the X-ray flux increases. There is evidence of a multi-colour disk with a temperature of $T_{in} \sim 70\,eV$ in the inner region at the beginning of the X-ray rising phase. The high-quality *XMM-Newton* data suggest that a warm and hot corona might cause the X-ray emission through inverse Comptonisation of soft disk seed photons during the plateau phase and at the bright end of the rising phase. (3) J0456−20 shows only moderate UV variability and no significant optical variability above the host galaxy level. Optical spectra taken at different X-ray phases are constant in time and consistent with a typical quiescent galaxy with no indication of emission lines. (4) Radio emission is (as yet) only detected in the X-ray plateau phase and rapidly declines on a timescale of two weeks.

Conclusions. J0456−20 is likely a repeating nuclear transient with a tentative recurrence time of ∼223 days. It is a new member of this rare class. We discuss several possibilities to explain the observational properties of J0456−20. We currently favour a repeating partial tidal disruption event as the most likely scenario. The long-term X-ray evolution is explained as a transition between a thermal disk-dominated soft state and a steep power-law state. This implies that the corona can be formed within a few months and is destroyed within a few weeks.

Key words. X-rays: individuals: eRASSt J045650.3−203750 – accretion, accretion disks – galaxies: nuclei – black hole physics

1. Introduction

Supermassive black holes (SMBHs) with masses $\sim 10^6$–$10^9\,M_\odot$ are thought to be ubiquitous in the centres of all massive galaxies (e.g. Kormendy & Richstone 1995; Magorrian et al. 1998). The tight correlation between the mass of the central black hole (BH) and the properties of the host galaxy observed in the local Universe (e.g. Ferrarese & Merritt 2000; Gebhardt et al. 2000) suggest a coevolution of SMBHs and their host galaxies (Kormendy & Ho 2013). Our understanding of the growth history and evolution of SMBHs (e.g. Merloni & Heinz 2013) mainly comes from the studies of SMBHs at the centres of active galactic nuclei (AGNs). However, AGNs only comprise a small fraction of the whole galaxy population. Our current understanding is that an AGN represents a particular phase in the evolution of a galaxy, during which the BH grows mainly through radiatively efficient accretion (Alexander & Hickox 2012). It is thus essential to study the BH demography from a large sample of quiescent galaxies, particularly covering low SMBH masses, and to study SMBHs with extremely low accretion rates, which cannot be explored easily in general AGN studies.

Occasionally, dormant SMBHs will be temporarily fuelled with a sudden influx of gas, which can be caused by ill-fated stars wandering too close to the SMBH. One such scenario comprises tidal disruption events (TDEs; Rees 1988; Evans & Kochanek 1989), in which a star enters the tidal radius of the SMBH and is torn apart by strong tidal forces. A fraction of the stellar debris falls inwards towards the SMBH. On the other hand, stars might also be on tightly bound orbits around the SMBHs with low eccentricities, resulting in extreme mass-ratio inspirals (EMRIs) undergoing stable Roche-lobe overflow (RLOF) onto the SMBHs. The mass-transfer rate is temporarily enhanced during grazing physical collisions between a pair of RLOFing EMRIs (Metzger & Stone 2017; Metzger et al. 2022). During these processes, a fraction of the influx of gas is eventually accreted onto the SMBH, producing energetic nuclear transients. The peak luminosity is in the range of a few percent to close to the Eddington luminosity ($L_{\rm Edd} \equiv 1.3 \times 10^{38} M_{\rm BH}/M_\odot\,{\rm erg\,s^{-1}}$), which is comparable to AGN luminosities. Thus nuclear transients provide an effective tool for discovering SMBHs in a large sample of otherwise quiescent galaxies.

Theoretical calculations have suggested that transitions between different accretion modes will take place when the accretion rate reaches certain critical values (Meyer et al. 2000). Evidence for transitions of the accretion flow in accreting BH systems, for instance, from a standard thin accretion disk (Shakura & Sunyaev 1973) dominated by thermal emission in the soft state to the advection-dominated accretion flow (ADAF; Narayan & Yi 1995; Yuan & Narayan 2014) in the hard state and vice versa, has been found mainly in stellar mass BH X-ray binaries (BHXRBs; see Remillard & McClintock 2006, for more details on the different accretion states in BHXRBs). It is thought that a steady compact jet, which is known to be associated with the hard state of BHXRBs, becomes unstable during the transition from the hard to soft state (Fender et al. 2004). On the other hand, powerful transient jets are often observed close to the peak of BHXRB outbursts (see Fender et al. 2004, for a review) during the transition from the hard to the soft state via the steep power-law state. However, strong observational evidence for an accretion-mode transition in individual AGN remains elusive, although it has been invoked to explain the large amplitude X-ray variability in a few AGNs (e.g. NGC 7589; Yuan et al. 2004; Liu et al. 2020) and changing-look AGNs (e.g. Noda & Done 2018). The Eddington ratio in nuclear transients can change by orders of magnitude on a timescale of hours to years, which is rarely seen in individual AGNs, providing an ideal laboratory for exploring the accretion process across a broad range of Eddington ratios. This might yield new insights into the launch of relativistic jets in BH–accretion systems.

A growing number of nuclear transients have been discovered in the past decades. Among them, TDEs are perhaps the most well known and well studied. The first TDE candidate was discovered in the soft X-ray band using archival ROSAT data (Komossa & Bade 1999, NGC 5905). After this, more candidates were found in the X-ray band from archival data (e.g. see Komossa 2015; Saxton et al. 2021, for reviews), and in the UV band using GALEX data (e.g. van Velzen et al. 2020). A few TDEs have also been discovered in the hard X-ray band (e.g. Swift 1644+57; Bloom et al. 2011; Levan et al. 2011; Zauderer et al. 2011) with the Neil Gehrels Swift Observatory (*Swift*). They can also be luminous in the radio band; the radio emission is thought to arise from relativistic jets launched by the TDEs (e.g. Zauderer et al. 2011, 2013). Radio emission from non-jetted TDEs has also been reported recently (van Velzen et al. 2016), which shed light on the type of outflows associated with both optical/UV and X-ray bright events (see Alexander et al. 2020, for a review). The advance in wide-field high-cadence optical surveys over the past decade, such as the All-Sky Automated Survey for Supernovae (ASAS-SN[1]), the Palomar Transient Factory (PTF; Law et al. 2009), the Panoramic Survey Telescope and Rapid Response System (Pan-STARRS; Chambers et al. 2016), the Zwicky Transient Facility (ZTF; Bellm et al. 2019), and the Asteroid Terrestrial-impact Last Alert System (ATLAS; Tonry et al. 2018), has not only greatly enlarged the number of known TDEs (e.g. van Velzen et al. 2020), but also facilitated the discovery of new classes of nuclear transients that cannot easily be explained by normal TDEs. One example is the new class of extremely energetic transients reported by Kankare et al. (2017). Trakhtenbrot et al. (2019) also presented a sample of AGNs that showed extreme flares. Malyali et al. (2021) reported a novel nuclear transient discovered by extended ROentgen Survey with an Imaging Telescope Array (eROSITA; Predehl et al. 2021) in a galaxy without an indication of prior activity. This transient shows double peaks in its optical light curve. TDEs and other unusual nuclear transients are also being discovered in the extremely dust-extincted luminous infrared galaxies in surveys targeting dust-obscured supernovae, which are infrared and radio bright, but faint or undetected at optical and X-ray wavelengths (e.g. Mattila et al. 2018; Kool et al. 2020).

Recently, a few transients with periodic or repeating flares in X-ray and/or optical/UV have been reported. Quasi-periodic eruptions (QPE) were first detected in the AGNs GSN 069 and RX J1301.9+2747 (Miniutti et al. 2019; Giustini et al. 2020). Recently, Arcodia et al. (2021) reported two more events, the eRO-QPE1 and eRO-QPE2 found in the first eROSITA All Sky Survey (eRASS1), in galaxies without optical signature of AGNs. These sources showed X-ray eruptions with X-ray flux increases of up to several orders of magnitude with a duration shorter than hours and a recurrence time shorter than one day. Periodic flares with a longer duration and recurrence time have also been discovered in optical bands. ASASSN-14ko is a periodic nuclear transient discovered by ASAS-SN in the Seyfert 2 AGN ESO 253-G003 (Payne et al. 2021). It flared at regular intervals over the past 7 years. The flares lasted for several

---

[1] https://www.astronomy.ohio-state.edu/asassn/index.shtml

months and recurred every ∼114 days. Repeating or periodic transients on much longer timescales (i.e. decades) are more challenging to discover with current surveys. Nevertheless, it has been suggested that the late-time X-ray re-brightening of IC 3599, a TDE candidate in a low-luminosity AGN discovered with ROSAT, might be caused by a repeating partial tidal disruption event (pTDE) with a recurrence time of 9.5 years (Campana et al. 2015, but see Grupe et al. 2015 for a different interpretation).

While our understanding of nuclear transients, particularly TDEs, has greatly improved through the enlarged samples, the nature of even the most well-studied nuclear transients can still be controversial (e.g. ASASSN-15lh; Zabludoff et al. 2021). Even less is known about the nature of periodic or repeating nuclear transients. Theoretical models involve collisions between a pair of EMRIs orbiting an SMBH (QPEs and ASASSN-14ko; Metzger et al. 2022) or a pTDE (ASASSN-14ko and IC 3599). On the other hand, the physical processes driving the multi-wavelength emission, which are crucial for understanding the nature of these nuclear transients, are still under hot debate. For instance, the detection of bright optical TDEs came as a surprise, since strong optical emission was not expected in early theoretical TDE work. It has been suggested that the optical emission may be caused by the reprocessing of the UV/X-ray emission by optically thick material (e.g. Dai et al. 2018), although others explained the optical emission as shocks generated through collisions of stellar streams (Piran et al. 2015; Lu & Bonnerot 2020). While the outflow properties of optical/UV and X-ray selected TDEs can also be probed by radio detections, the source of the radio emission is also debated, including scenarios such as collision-induced spherical outflows (e.g. Goodwin et al. 2022) or accretion-driven winds (e.g. Alexander et al. 2016; Cendes et al. 2021), or a collimated sub-relativistic jet (e.g. van Velzen et al. 2016; Cendes et al. 2022). However, it is currently unclear whether the X-ray and optical/UV selected TDEs are populations that are intrinsically different because the sample of X-ray selected nuclear transients is still relatively small. Systematic multi-wavelength studies of an X-ray selected sample can afford us new insights into the nature of these nuclear transients (e.g. Sazonov et al. 2021).

In this paper, we present the discovery of a likely repeating nuclear transient, eRASSt J045650.3−203750 (hereafter J0456−20), discovered in eRASS2 in a quiescent galaxy at a redshift of $z \sim 0.077$. During its all-sky survey, eROSITA rapidly uncovers transients associated with the nuclei of galaxies that show no apparent signatures of prior AGN activity. J0456−20 is one of the most variable X-ray sources in this sample (see Fig. 1), showing a drastic X-ray flux drop by a factor of 100 within one week. Our follow-up optical spectroscopic observations revealed optical spectra typical of a quiescent galaxy, without signatures of emission lines. More importantly, the long-term X-ray and UV light curves suggest that J0456−20 likely is a repeating nuclear transient with a roughly estimated recurrence time of 223 days. This adds a member to this rare nuclear transient class. Transient radio emission is also detected in J0456−20, indicating that an outflow or jet may have been launched during its cycle. This paper is structured as follows. In Sect. 2 we describe the multi-wavelength data reduction. Our optical spectroscopic analysis, X-ray/UV temporal study, radio data analysis, and X-ray spectral modelling, and short-term variability analysis are presented in Sect. 3. Finally, we discuss and summarise our results in Sects. 4 and 5.

Throughout this paper, we adopt a flat ΛCDM cosmology with $H_0 = 67.7 \,\mathrm{km\,s^{-1}\,Mpc^{-1}}$ and $\Omega_m = 0.308$ (Planck Collaboration VI 2020). Therefore, $z = 0.077$ corresponds to a luminosity distance of $D_{\mathrm{ld}} = 360 \,\mathrm{Mpc}$. All magnitudes are reported in the AB system (not corrected for Galactic extinction).

2. Observations and data reduction

J0456−20 was discovered by eROSITA in eRASS2 and was detected in all subsequently performed all-sky scans, eRASS3 and eRASS4. An extensive multi-wavelength follow-up campaign was organised. It is described in this section.

2.1. eROSITA

We first discovered J0456−20 in its faint X-ray state in a dedicated search for TDE candidates in eRASS2, which consists of ten consecutive eROSITA scans at the location of J0456−20 with gaps of ∼4 h each between 2020 September 8 and 10. J0456−20 was not detected in eRASS1, which covered the location of the source between 2020 March 10 and 11. It was detected again in eRASS3 and eRASS4 with an X-ray flux higher by ∼25 and ∼10 times than in eRASS2, respectively. The eRASS3 observation was split into two segments because of an orbit correction performed by the Spectrum-Roentgen-Gamma (SRG; Sunyaev et al. 2021) spacecraft, followed by a test of the cooling system of the CCD cameras. The first segment was performed between 2021 February 27 and 2021 February 28, and the second segment was carried out ∼8 days later, between 2021 March 8 and 9. eROSITA observed the source again during eRASS4 between 2021 September 2 and 4. The position of the X-ray transient measured from eRASS3 is (RA, Dec) = (04:56:49.74, −20°37′48.44″) with an uncertainty of 1.0″. An optical source at an angular distance of 1.0″ with coordinates (04:56:49.80, −20°37′47.99″) is identified as the optical counterpart. A false-colour image of the host galaxy, overlaid with positions measured from different instruments, is shown in Fig. A.1.

All eROSITA data were calibrated and cleaned using the pipeline version 946 of the eROSITA Science Analysis Software (eSASS; Brunner et al. 2022). The photon events from all seven telescopes were merged into one event-list file. The SRCTOOL in eSASS (version 20211004) was used to extract the X-ray spectra and light curves. A circular region with a radius of 50″ was chosen as the source region for eRASS3 and eRASS4. However, a smaller source region with a radius of 30″ was chosen for eRASS2 to increase the signal-to-noise ratio (S/N) as the source is very faint during the eRASS2 observation. J0456−20 is not detected in eRASS1, so for that epoch we used the source region defined for eRASS2. A source-free annular region with an inner radius of 90″ and outer radius of 120″ was selected as the background region for all the eROSITA observations. Assuming a model consisted of an absorbed power-law (TBabs*zashift*cflux*powerlaw in XSPEC, hereafter M_{ul}) with a photon index fixed at 3.0 and the Galactic absorption ($N_{\mathrm{H,Gal}}$) fixed at 3.3×10^{20} cm^{-2} (Willingale et al. 2013), we estimated a 3σ upper limit of 2.2×10^{-13} erg cm^{-2} s^{-1} in the 0.2−2.0 keV energy band for eRASS1 (see Appendix B). For all the other eRASS observations, the X-ray flux was estimated via X-ray spectral modelling. More details about the eROSITA observations are listed in Table C.2.

2.2. XMM-Newton

Pre-approved *XMM-Newton* target of opportunity (ToO) observations were performed on 2021 March 27 (Obs-ID:
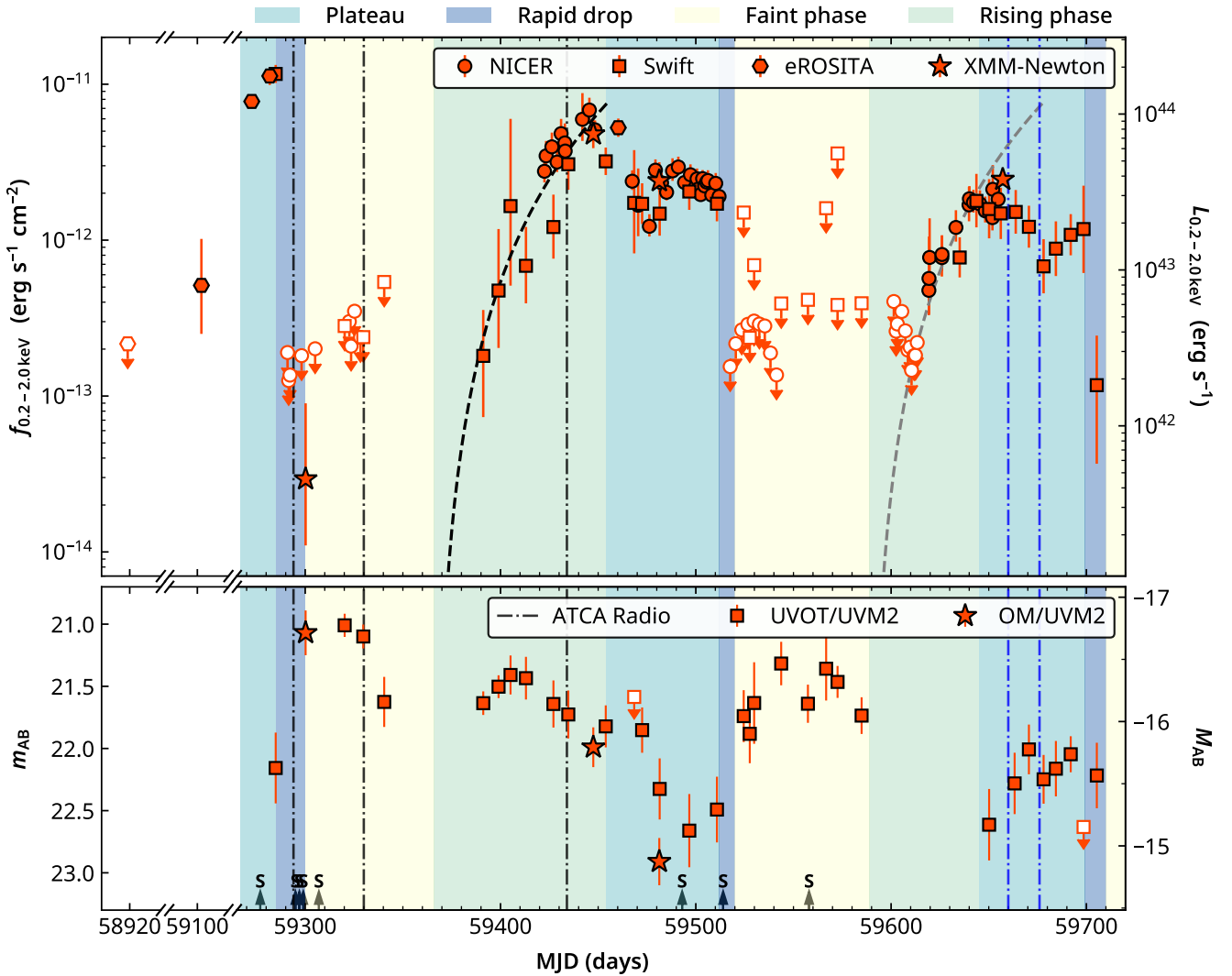
Fig. 1. Long-term X-ray and UV light curves for J0456−20. The coloured regions represent the four phases defined in Sect. 3.1 based on the X-ray light curve: the plateau phase ($P_{\mathrm{X,plat}}$, light cyan), the rapid drop phase ($P_{\mathrm{X,drop}}$, light blue), the faint phase ($P_{\mathrm{X,faint}}$, light yellow), and the rising phase ($P_{\mathrm{X,rise}}$, light green). *Upper panel:* Red points are the unabsorbed intrinsic 0.2−2.0 keV X-ray light curve from eROSITA (hexagons), *Swift*/XRT (squares), NICER (circles), and *XMM-Newton* (stars). The error bars indicate 90% uncertainties. The 3σ flux and luminosity upper limits are shown with downward arrows. The dashed black line shows the best-fitting power-law model, $f_{\mathrm{rs}}(t) \propto (t - t_0)^\beta$, where $t_0 = 59377 \pm 9$ and $\beta = 2.3 \pm 0.7$ (quoted uncertainties are at 1σ confidence level), during the rise phase. The dashed grey line shows the same model, but shifted by 223 days. *Bottom panel:* Long-term UV light curves from *Swift*/UVOT UVM2 (red squares) and *XMM-Newton*/OM UVM2 (red stars). The error bars mark the 1σ uncertainties. Empty squares with downward arrows indicate 3σ upper limits. The vertical dashed-dotted lines mark the dates of the five ATCA radio observations (black: non-detections; blue: detections), and the upward arrows marked with an S indicate the dates when optical spectra were obtained.

0862770201, hereafter X1; PI: Krumpe) and 2022 March 19 (Obs-ID: 0884960601, hereafter X4; PI: Liu). In addition, we requested two longer *XMM-Newton* Director's Discretionary Time (DDT) observations performed on 2021 August 21 and September 21 (PI: Liu; Obs-IDs: 0891801101 and 0891801701, hereafter X2 and X3, respectively) to investigate the short-term X-ray variability. The details of the *XMM-Newton* observations are listed in Table C.2.

All *XMM-Newton* data were reduced using the latest calibration files. The observation data files (ODFs), retrieved from the *XMM-Newton* Science Archive, were reduced using the *XMM-Newton* Science Analysis System software (SAS, version 19.1; Gabriel et al. 2004). For each observation, the SAS tasks EMCHAIN and EPCHAIN were used to generate the event lists for the European Photon Imaging Camera (EPIC)

MOS (Turner et al. 2001) and pn (Strüder et al. 2001) detectors, respectively. High-background flaring periods were identified and filtered from the event lists. J0456−20 is detected in all the *XMM-Newton* observations except for X1 in the standard source detection pipeline using edetect_chain. However, we detected J0456−20 in X1 with ML_DET of 11.8 in a customised pipeline, during which the source detection edetect_chain task was run on the combined MOS1 and MOS2 data over the 0.2−1.0 keV band. To increase the S/N, we selected a circular region with a radius of 15″ as the source region for the MOS1 and MOS2 images for X1. A larger circular region with a radius of 45″ was chosen for the MOS1, MOS2, and pn images for all the other observations. A source-free circular region with a radius of 100″ was chosen as the background region for the MOS cameras. The background region for the pn camera

was selected from a circular region with a radius of 60″ centred at the same CCD read-out column as the source position. X-ray events with pattern ≤12 for MOS and ≤4 for pn were selected to extract the X-ray spectra. We used the SAS task RMFGEN and ARFGEN to generate the response matrix and ancillary files, respectively. We only extracted the X-ray spectra from the MOS1 and MOS2 data for X1. They were combined into one MOS spectrum using the ADDASCASPEC task to increase the S/N, and were then rebinned to have at least one count in each energy bin. For all the other observations, the X-ray spectra (MOS1, MOS2, and pn) were rebinned to have at least 20 counts for each background-subtracted channel and to avoid oversampling the intrinsic energy resolution by a factor larger than 3.

The *XMM-Newton* Optical Monitor (OM) observations were taken in image+fast mode using the UVM2 filter. The OM imaging- and fast-mode data were analysed using the omichain and omfchain tasks, respectively. The fast-mode data are dominated by background because the source is faint in the UV. Only the image-mode data were therefore used. J0456−20 is detected in the OM/UVM2 data in all four observations, except for X4. We only report the OM/UVM2 results for the three observations in which J0456−20 is detected. We found no significant short-term UVM2 variability in any of the three observations. We thus report the OM/UVM2 photometry using the combined OM data set of the three observations. The measured AB magnitudes and flux densities for each observation are listed in Table C.1.

2.3. Swift observations

An extensive X-ray and UV follow-up campaign of J0456−20 was performed with *Swift* (PIs: Krumpe & Liu). Three *Swift* observations (obsids: 00014135030, 00014135031, 00014135032) were observed within 2 days. We therefore stacked these three observations, and assign this stacked observation the surrogate ObsID 00014135999 for the purpose of brevity in Tables C.1 and C.2. We used the XRT (X-Ray Telescope) online data analysis tool[2] (Evans et al. 2009) to check whether the source was detected for each individual observation (for more details about the XRT source detection, see Evans et al. 2020). For observations in which the source was detected, we used the same online tool to generate the X-ray spectra. The X-ray flux was then calculated through X-ray spectral fitting. For observations in which the source was not detected, we obtained the total and background photon counts as well as the 3σ count rate upper limits using the XRT online tool. The M_{ul} model was then used to convert the count rate upper limits into the 0.2−2.0 keV flux upper limits.

The *Swift* Ultraviolet/Optical Telescope (UVOT) data were reduced using the UVOT analysis pipeline provided in HEASOFT with the UVOT calibration version 20201215. Source counts were extracted from a circular region with a radius of 5″ centred at the source position, and a 20″ radius circle was chosen as the background region centred at a source-free region close to the position of J0456−20. The task UVOTSOURCE was used to perform photometric measurements. We confirmed the overall accuracy of the photometric measurements with a nearby star. The standard deviation derived from the star is about 0.1 mag, which is smaller than the typical UVOT uncertainty for J0456−20. We further verified that small-scale sensitivity (SSS) does not affect the UVOT data at the position of J0456−20. A summary of the *Swift*/UVOT observations is listed in Table C.1.

2.4. NICER observations

The monitoring of J0456−20 with the Neutron star Interior Composition Explorer (NICER; Gendreau et al. 2016) was triggered shortly after the eRASS3 detection (PIs: Liu & Krumpe). The NICER data were analysed using the heasoft software (version 6.29c) with the latest calibration files (version 250210707). Data were downloaded from the NICER data archive on HEASARC. Noisy detectors were excluded for each observation by running a 5σ clipping on all 52 detectors. The merged level 2 event-list file for the remaining detectors were regenerated following the standard nicerl2 pipeline[3]. The background and total X-ray spectra were then generated using the BACKGEN3C50 pipeline[4]. Following the suggestion from Remillard et al. (2022), additional selection criteria were applied to exclude periods during which $S0_{net}$ is higher than 2 and hbg_{net} is higher than 0.05. The nicerarf and nicerrmf tasks were used to generate the response matrix and ancillary file for each observation[5], respectively.

The NICER background spectra were generated using an empirical background model (Remillard et al. 2022) with a Gaussian uncertainty rather than a Poisson uncertainty. The NICER data are also often dominated by systematic uncertainties. We therfore calculated the 3σ photon count upper limits for NICER using the following formula: $N_{3\sigma} = 3\sqrt{N_{bkg} + (N_{bkg} \times \sigma_{sys})^2}$, where N_{bkg} is the total background photon count in a given energy range, and σ_{sys} is the systematic uncertainty. In this work, we estimated the 3σ photon count upper limits for NICER non-detections over the 0.4−1.0 keV band[6] with a systematic uncertainty of $\sigma_{sys} = 0.05$. Observations with $N_{tot,0.4−1.0\,keV} > N_{bkg} + N_{3\sigma}$ were considered as detected. For observations in which J0456−20 was detected, the NICER X-ray spectra were then rebinned using the ftgrouppha tool with the optimal binning scheme from Kaastra & Bleeker (2016) and a minimum photon count of 20 per bin. The X-ray flux was then estimated through X-ray spectral modelling (Sect. 3.3.3). For non-detections, the M_{ul} model was again used to convert the 3σ count rate upper limits ($N_{3\sigma}/t_{exposure}$) into the 0.2−2.0 keV flux upper limits.

2.5. Optical spectroscopic observations

We performed several optical spectroscopic follow-up observations of the optical counterpart of J0456−20. The observations were made from early March 2021 until the end of 2021 (Table 1) and are marked in Fig. 1.

SALT: Two pairs of optical spectra, both 200 s exposure, were obtained using the RSS instrument (Burgh et al. 2003) on the Southern African Large Telescope (SALT; Buckley et al. 2006), on the night of 2021 March 4. We used the PG0900 grating and a slit width of 1.5″. The first pair of spectra covered the wavelength range 3636−6699 Å, and the second pair

---

[2] http://www.swift.ac.uk/user_objects

[3] https://heasarc.gsfc.nasa.gov/docs/nicer/analysis_threads/nicerl2

[4] https://hera.gsfc.nasa.gov/docs/nicer/tools/nicer_bkg_est_tools.html

[5] J0456−20 was very faint (close to the sensitivity limit) during NICER observation 4595020126, which consists of seven snapshots. J0456−20 was detected in three snapshots, but it was not detected in the other four snapshots, likely because of the short exposure time and/or background variability. In this work, we report the results from the three detection snapshots for this observation.

[6] This energy range was chosen to avoid potential contamination from optical loading in the energy band below 0.4 keV.

of redder spectra covered 6031−8981 Å, both at a resolution of 5.5 Å. Sky conditions were clear, with a seeing of ~1.2″. To reduce the spectra, we used the PyRAF-based PySALT package[7] ([Crawford et al. 2010](#)), which includes corrections for gain and cross-talk and performs bias subtraction. We extracted the science spectrum using standard IRAF[8] tasks, including wavelength calibration (neon and argon calibration lamp exposures were taken, one immediately before and one immediately after the science spectra, respectively), background subtraction, and one-dimensional spectrum extraction. The pupil (i.e. the view of the mirror from the tracker) moves during all SALT observations, causing the effective area of the telescope to change during exposures. Therefore, no absolute flux calibration is possible. However, by observing spectrophotometric standards during twilight, we were able to obtain relative flux calibration, allowing the recovery of the correct spectral shape and relative line strengths.

NTT: The source was observed with the ESO Faint Object Spectrograph and Camera v.2 (EFOSC2; [Buzzoni et al. 1984](#)) mounted on the ESO New Technology Telescope (NTT) on 2021 March 26 (proposal ID 106.21RU.001, PI: Malyali). We used grism 13 and the 1.2″ slit oriented 11 degrees off the parallactic angle. We obtained two consecutive exposures of 1800 s each with a seeing of about 1″ during the observation. The spectrum has a wavelength range of 3685−9315 Å with a dispersion of 2.77 Å/pixel. The data were reduced and calibrated using the `esoreflex` pipeline ([Freudling et al. 2013](#), v2.11.5). The He+Ar arcs were used to obtain the wavelength calibration, and the standard star LTT3864 was used for flux calibration, which was observed with the same grism and the same slit oriented along the parallactic angle.

FORS2: We observed J0456−20 with the FORS2 instrument ([Appenzeller et al. 1998](#)) on UT1 of the Very Large Telescope Array on 2021 April 3 (proposal ID 106.21RU, PI: Krumpe). We used grisms 300V and 300I (+OG590 filter), with combined exposure times of 1000 s per grism. We made use of a 1.3″ slit under clear observing conditions. All reductions and calibrations of the data were performed using the `esoreflex` pipeline (v2.11.3). We made use of He+HgCd+Ar (300V) and He+Ar (300I) arcs for the wavelength calibration and used observations of the flux standard LTT4816, which was observed using the same instrumental set-up.

Gemini: This target was observed with the GMOS-S Hamamatsu detectors in two seasons in 2021 March and 2021 October. The data were reduced using the Python spectroscopic data reduction pipeline (PypIt; [Prochaska et al. 2020](#)) tool. The CuAr arc lamp was used for the wavelength calibration, and the standard star EG274 was taken for flux calibration.

Magellan: A long-slit spectrum was obtained on 2021 October 26 with LDSS3-C mounted at Clay. The VPH-All grism was used in combination with a 1″ slit to cover a wavelength range of 3700−10 000 Å with a dispersion of about 2 Å/pixel and a resolution of about 8.5 Å. The slit was oriented along the parallactic angle. 3 × 600 s consecutive exposures were acquired to effectively remove cosmic rays. The seeing during the observation was around 0.5″. The spectra were reduced with IRAF following the usual procedure of overscan subtraction, flat-field correction, and wavelength calibration by means of a He-Ne-Ar lamp. The flux calibration was performed through the observation of the

[7] `https://astronomers.salt.ac.za/software/pysalt-documentation`
[8] `https://iraf.net`

Table 1. Spectroscopic observations of J0456−20.

UT date	Tel.	Inst.	Exp (ks)	Slit (″)	Airmass
2021-03-04	SALT	RSS	0.2	1.5	1.32
2021-03-22	Gemini	GMOS	0.3	1.0	1.43
2021-03-22	Gemini	GMOS	0.3	1.0	1.35
2021-03-27	NTT	EFOSC2	3.6	1.2	1.33
2021-04-03	VLT	FORS2	1.0	1.3	1.30
2021-10-06	Gemini	GMOS	0.3	1.0	1.30
2021-10-27	Magellan	LDSS3-C	1.8	1.0	1.10
2021-12-10	ANU	WiFeS	2.4	–	1.02

standard star LTT 9239. The same aperture slit was used, again oriented along the parallactic angle. Finally, the three exposures were sky subtracted and averaged to obtain the spectrum of the source.

WiFeS: We obtained a spectrum of J0456−20 with the Wide Field Spectrograph (WiFeS; [Dopita et al. 2010](#)) mounted on the ANU 2.3 m telescope at Siding Spring Observatory on 2021 December 10 (proposal ID 4210177, PI: Miller-Jones). We used the R3000 and B3000 gratings and obtained a NeAr arc lamp exposure after the target exposure. The total spectral range is from 3500 to 9000 Å. The data were reduced using the PyWiFeS reduction pipeline ([Childress et al. 2014](#)). The pipeline produces three-dimensional sets consisting of spatially resolved, bias subtracted, flat-fielded, wavelength- and flux-calibrated spectra for each slitlet. We then extracted background-subtracted spectra from the slitlets that provided the most significant flux using the task `apall` in IRAF. We used the white dwarf EG21 as the flux standard.

Overall, we found that the optical spectra are consistent with a typical quiescent galaxy with no indication of strong evolution or emission lines (see the left panel of Fig. [2](#)). We also extracted the optical light curves at the position of J0456−20 from the ATLAS and ZTF database. No significant optical variability was found. We measured a redshift of $z = 0.077$ in all spectra for J0456−20.

2.6. ATCA radio observations

We observed the position of J0456−20 with the Australia Telescope Compact Array (ATCA) radio telescope on five occasions between 2021 March and 2022 April at 2−21 GHz (project code C3334; PI: Anderson). All data were reduced in the Common Astronomy Software Application (CASA v5.6.3, [McMullin et al. 2007](#)) using standard procedures including flux and band-pass calibration with PKS 1934−638 and phase calibration with PKS 0454−234. Images of the target field of view were created using the CASA task `tclean`, and the flux density of the source was extracted in the image plane by fitting an elliptical Gaussian fixed to the size of the synthesised beam using the CASA task `imfit`.

No radio emission was detected at the location of J0456−20 in three observations during 2021 at either 5.5 or 9 GHz. However, on 2022 March 22, we detected a point source at both 5.5 and 9 GHz. The coordinates of the radio source are (RA, Dec) = 04h56m49.7s, −20°37′47.4″, measured from the 9 GHz data. The positional uncertainty is characterised by an ellipse with a semi-minor axis of 0.1″, a semi-major axis of 0.87″, and a rotation angle of 155°. We subsequently triggered a follow-up
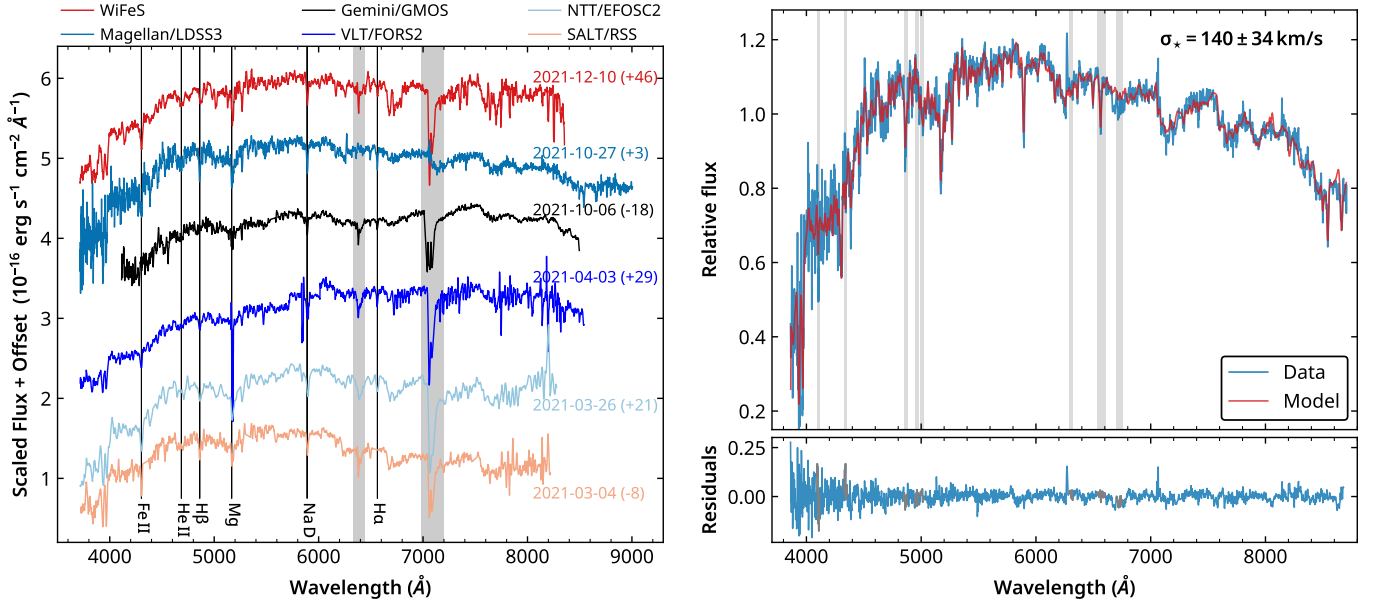
Fig. 2. Optical spectroscopic observations of J0456−20 and stellar velocity measurement. *Left panel:* The optical spectra are rescaled and shifted for illustration purposes. The values quoted in parentheses are the offset between the date of the optical observation and the date of the closest rapid X-ray flux drop, in units of days. The Magellan LDSS3-C spectrum is corrected for telluric absorption. *Right panel:* Magellan LDSS3-C rest-frame spectrum is shown with a solid dark blue line, and the solid red line shows the best-fitting model using the pPXF package. The blue lines at the bottom are the fit residuals, and the grey points and shadows mark the regions that are excluded from the fitting. We measured an intrinsic velocity dispersion of $140 \pm 34 \, \mathrm{km \, s^{-1}}$ from the Magellan data. We also measured the intrinsic velocity dispersion using the WiFeS data, which have a higher resolution than the Magellan LDSS3-C data. The intrinsic velocity dispersion obtained from the WiFeS data is $120 \pm 20 \, \mathrm{km \, s^{-1}}$, which is consistent with that from the Magellan data (see Sect. 3.4.1).

Table 2. ATCA radio observations of J0456−20.

Date	Frequency (GHz)	Array config.	Flux density (μJy)
2021-03-21	5.5	6D	<78
	9		<66
2021-04-26	5.5	6D	<36
	9		<47
2021-08-07	5.5	EW367	<125
	9		<57
2022-03-22	5	6A	257 ± 11
	6		278 ± 11
	9		311 ± 12
2022-04-06	2.1	6A	<738
	5.5		61 ± 18
	9		103 ± 23
	17		117 ± 22
	21		<198

Notes. Upper limits are reported at 3σ.
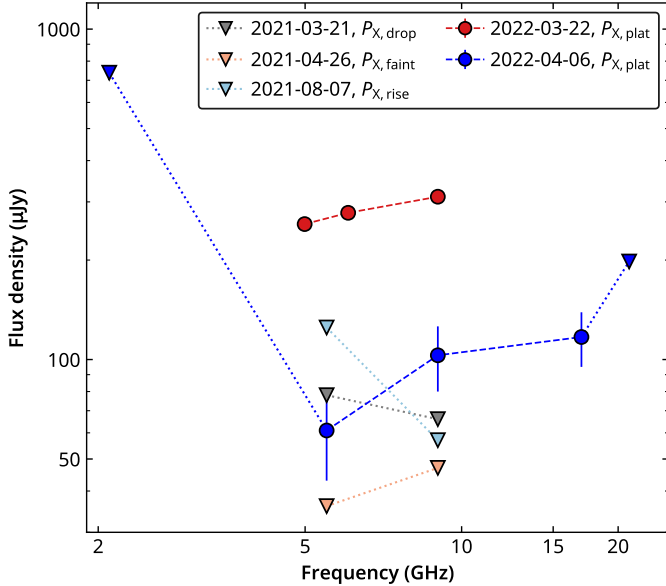

Fig. 3. ATCA radio observations of J0456−20. Filled circles with error bars (1σ uncertainties) represent the observed radio flux densities at different frequencies. Downward triangles indicate the 3σ upper limits. J0456−20 is detected only in the $P_{X,\mathrm{plat}}$ phase (blue and red).

self-calibration of the target field. The ATCA radio observations are summarised in Table 2.

To assess the possibility of short-time variability of the radio emission, we extracted the 5.5 and 9 GHz flux densities of J0456−20 when the source was brightest, on 2021 March 22, for individual 10-min scans. There is no statistically significant variability between the six scans we analysed. The probability of the flux density at each frequency is constant at $P = 0.95$ (5.5 GHz) and $P = 0.6$ (9 GHz).

observation at 2.1, 5.5, 9, 17, and 21 GHz on 2022 April 6 to characterise the radio spectrum of the transient (see Fig. 3). A point source around the location of J0456−20 is detected at 5.5, 9, and 17 GHz. Unfortunately, the 2.1 GHz field of view contains a bright AGN just outside of the primary beam, which hindered the deconvolution process and led to high image noise, even after

Table 3. Characteristics of the four different X-ray phase.

X-ray phase		Duration	$f_{X,soft}$ [a]	UV	Radio
$P_{X,drop}$	1st	$\lesssim$2 weeks	$2.9^{+6.0}_{-1.8} \times 10^{-14}$	Sudden rise	Non-detection
	2nd	$\lesssim$1 weeks	$<1.5 \times 10^{-13}$	Sudden rise	...
	3rd	$\lesssim$1 weeks	$1.2^{+1.3}_{-0.8} \times 10^{-13}$	Sudden rise	...
$P_{X,faint}$	1st	$\lesssim$3 months	$<1.0 \times 10^{-13}$	Bright	Non-detection
	2nd	$\lesssim$3 months	$<0.6 \times 10^{-14}$	Bright	...
$P_{X,rise}$	1st	$\gtrsim$2 months	$\sim6.8 \times 10^{-12}$	Rising, then decline	Non-detection
	2nd	$\gtrsim$1 months	$\sim2.0 \times 10^{-12}$	...	...
$P_{X,plat}$	1st	...	$\sim1.0 \times 10^{-11}$	...	...
	2nd	$\sim$2 months	$\sim2.3 \times 10^{-12}$	Decline	...
	3rd	$\sim$2 months	$\sim1.5 \times 10^{-12}$	Plateau	Rapid decline

Notes. Ellipsis dots mean that no observations or measurements are available. [a] $f_{X,soft}$ is the intrinsic 0.2–2.0 keV flux in units of erg cm^{-2} s^{-1}. For the $P_{X,plat}$ phase, $f_{X,soft}$ denotes the average flux in the $P_{X,plat}$ phase.

3. Data analysis and results

3.1. Long-term multi-wavelength light curves

We show the long-term X-ray/UV light curves of J0456−20 in Fig. 1. The unabsorbed rest-frame 0.2–2.0 keV X-ray flux ($f_{X,soft}$) was calculated from X-ray spectral modelling (see Sect. 3.3). We also show the time evolution of the radio spectra of J0456−20 in Fig. 3. J0456−20 is detected only in the X-ray plateau phase in the latest two radio observations.

It is clear from Fig. 1 that J0456−20 showed a drastic drop of the X-ray flux by more than a factor of $\gtrsim$100 ($\sim$300) within about one week (two weeks). By contrast, the UV only showed moderate variability, with $\Delta m \approx 1.5(0.8)$ mag on a much longer timescale of several months (three weeks). Subsequent X-ray/UV follow-up observations revealed that the source showed repeating and complicated long-term X-ray variability. We divided the long-term temporal evolution of J0456−20 into four phases based on the X-ray light curve: the rapid flux drop phase ($P_{X,drop}$), the faint phase ($P_{X,faint}$), the rising phase ($P_{X,rise}$), and the plateau phase ($P_{X,plat}$). The phases are represented with different background colours in Fig. 1. In Fig. 1 we also indicate the times of the ATCA observations. We summarise the multi-wavelength characteristics of each phase below (see also Table 3).

3.1.1. Rapid X-ray flux drop phase $P_{X,drop}$

The most prominent temporal feature of J0456−20 is the drastic X-ray flux drop that occurred shortly after the eRASS3 and first *Swift* (hereafter Swift1) observations around MJD 59290, during which $f_{X,soft}$ dropped from $\sim1.2 \times 10^{-11}$ erg cm^{-2} s^{-1} to a 3σ upper limit of $\sim1.3 \times 10^{-13}$ erg cm^{-2} s^{-1} (measured from NICER observations) in 7 days. A faint source is detected in X1, which was taken $\sim$15 days after Swift1, with $f_{X,soft}$ = $3^{+6}_{-2} \times 10^{-14}$ erg cm^{-2} s^{-1} (see Sect. 3.3.3). A second $P_{X,drop}$ phase occurred $\sim$223 days later around MJD 59514, when the $f_{X,soft}$ dropped by a factor of $>$ 10 in 6 days. A third $P_{X,drop}$ likely occurred at MJD 59698, about 408 days after Swift1, in which $f_{X,soft}$ decreased from $1.2^{+1.1}_{-0.6} \times 10^{-12}$ erg cm^{-2} s^{-1} to $1.2^{+1.3}_{-0.8} \times 10^{-13}$ erg cm^{-2} s^{-1} in 7 days. Confirmation from subsequent X-ray observations was not possible because J0456−20 was blocked by the Sun.

The UV variability, however, is very different from the X-ray during the $P_{X,drop}$ phase. Although we only have sparse UV coverage during the $P_{X,drop}$, it is likely that the observed

three $P_{X,drop}$ phases all began at the time when the UV was faint, with UVOT/UVM2 magnitudes of 22.2 ± 0.3, 22.5 ± 0.3, and <22.6 mag at the start of the first, second, and third $P_{X,drop}$, respectively. In contrast to the X-ray band, the UV brightness increased during the $P_{X,drop}$ phase.

We observed J0456−20 in the radio bands with ATCA soon after the X-ray flux drop (e.g. $\sim$10 days after Swift1) during the first $P_{X,drop}$ phase. No significant radio emission was detected at the position of J0456−20 with 3σ upper limits of 78 and 66 µJy in the 5.5 and 9 GHz bands, respectively.

3.1.2. X-ray faint phase $P_{X,faint}$

Immediately after the $P_{X,drop}$ phase, J0456−20 was not detected in the X-ray band for about two months (hereafter the $P_{X,faint}$ phase), with a 3σ flux upper limit as low as $\sim1.0 \times 10^{-13}$ erg cm^{-2} s^{-1} in the NICER and *Swift* monitoring programs. Combining all the *Swift*/XRT non-detections during the first and second $P_{X,faint}$ phases, we obtained 3σ upper limits of ~1.0 and $\sim0.6 \times 10^{-13}$ erg cm^{-2} s^{-1} with total exposures of 7998 and 17393 seconds, respectively. We obtained a slightly lower 3σ $f_{X,soft}$ upper limit of $\sim4.2 \times 10^{-14}$ erg cm^{-2} s^{-1} for the $P_{X,faint}$ phase by combining all the *Swift*/XRT non-detections. Using the current data set, we estimate that the $P_{X,faint}$ phase lasted between 60 and 90 days.

Whilst the X-ray became considerably fainter, the UV rose to its brightest magnitude, with $m_{UV} = 21.0 \pm 0.1$ and 21.3 ± 0.2 observed during the first and second $P_{X,faint}$ phase, respectively. The UV brightness shows an initial rise in the second $P_{X,faint}$ phase, followed by an overall decline.

We observed J0456−20 with ATCA in the 5.5 and 9 GHz bands during the first $P_{X,faint}$ phase. The radio observation was carried out quasi-simultaneously with one of the *Swift* observations during which the UV was fairly bright, with $m_{UV} = 21.1 \pm 0.1$. We did not detect significant radio emission at the position of J0456−20 with 3σ upper limits of 36 and 47 µJy in the 5.5 and 9 GHz bands, respectively.

3.1.3. X-ray rising phase $P_{X,rise}$

The two $P_{X,rise}$ phases, both following a $P_{X,faint}$ phase, were well captured by our *Swift* and NICER monitoring with an observed faintest $f_{X,soft}$ of $1.8^{+1.7}_{-1.1} \times 10^{-13}$ erg cm^{-2} s^{-1}. To characterise the profile of the X-ray light curve during the $P_{X,rise}$
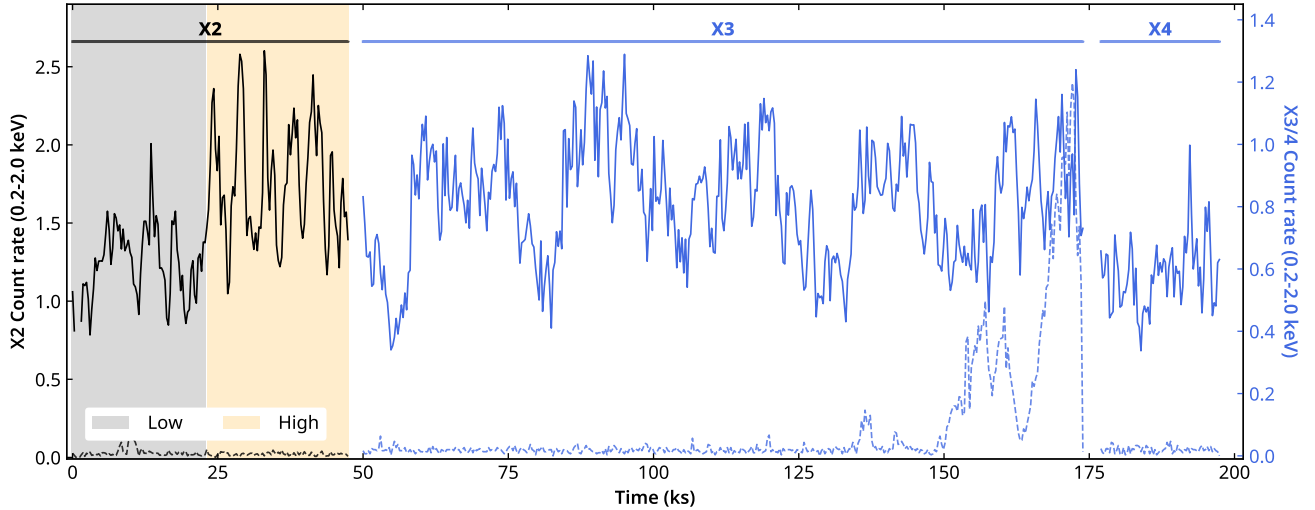
Fig. 4. *XMM-Newton* pn light curve in the 0.2−2.0 keV energy range, with a bin size of 300 s. The solid and dotted lines show the source and background light curves, respectively. The light curves for X2 are shown in black, and the blue lines show the light curves for X3 and X4. The high-background flare in the last 27 ks of X3 is clearly visible. This high-background period is excluded from our temporal and spectral analysis. The time intervals we used to extract the X-ray spectra in the high- and low-flux state of X2 are marked in orange and grey, respectively.

phase, we modelled the first $P_{X,rise}$ phase X-ray light curve (MJD 59390–59460) with a power-law function $f_{rs}(t) = A * (t - t_0)^\beta$. The Python package `emcee` was used to estimate the uncertainties. We obtained a best-fitting index of ∼2.3 ± 0.7 and t_0 = MJD 59377 ± 9. Interestingly, this best-fitting power-law function can match the light curve profile of the second $P_{X,rise}$ phase very well by simply shifting t_0 by ∼223 days (see Fig. 1). In contrast, the peak $f_{X,soft}$ in the second $P_{X,rise}$ phase (∼2.0 × 10^{-12} erg cm^{-2} s^{-1}) is fainter than that in the first phase (∼6.8 × 10^{-12} erg cm^{-2} s^{-1}). We also note that significant short-term X-ray variability is clearly detected in the *XMM-Newton* observation (Fig. 4) at a time close to the peak X-ray flux in the $P_{X,rise}$ phase. The second $P_{X,rise}$ phase (≳30 days) is ∼30 days shorter than the first phase.

The UV light curve is well sampled only in the first $P_{X,rise}$ phase. J0456−20 is generally relatively bright in the UV band during the $P_{X,rise}$ phase. The UV was initially in a rising phase, which is similar to the X-ray, followed by a decline, while the X-ray flux continued to increase. However, this cannot be confirmed in the second $P_{X,rise}$ phase because we lack UV observations.

A radio observation by ATCA was carried out quasi-simultaneously with the X-ray/UV observation during the first $P_{X,rise}$ phase. We again did not detect significant radio emission at the position of J0456−20, with 3σ upper limits of 125 and 57 μJy in the 5.5 and 9 GHz bands, respectively. We note that J0456−20 was in a fairly X-ray bright state with $f_{X,soft}$ of ∼3.0 × 10^{-12} erg cm^{-2} s^{-1} at the time of the ATCA observation.

3.1.4. X-ray plateau phase $P_{X,plat}$

Following the first and second $P_{X,rise}$ phases, the X-ray flux of J0456−20 was stable within a factor of 2 for abouttwo months (the $P_{X,plat}$ phase) during MJD 59454–59512 and 59645–59699 (Fig. 1) before it transited to the $P_{X,drop}$ phase. During the $P_{X,plat}$ phases, significant short-term variability by a factor of 2 on a timescale of a few hours (Fig. 4) was seen in the *XMM-Newton* observations. The $f_{X,soft}$ observed in the two eRASS3 segments (7.8 ± 0.8 × 10^{-12} and 1.1$^{+0.2}_{-0.1}$ × 10^{-11} erg cm^{-2} s^{-1}) and the Swift1 observation (1.2$^{+0.2}_{-0.1}$ × 10^{-11} erg cm^{-2} s^{-1}) are very similar. In addition, their X-ray spectral properties (discussed below) are

also consistent with the properties observed in the $P_{X,plat}$ phase. We thus concluded that J0456−20 was in the $P_{X,plat}$ phase during the eRASS3 and Swift1 observations (MJD 59272–59285, the first observed $P_{X,plat}$ phase). The average 0.2−2.0 keV flux in each $P_{X,plat}$ phase showed a monotonic decrease. Compared to the first $P_{X,plat}$, the average $f_{X,soft}$ decreased by a factor of ∼4 and 7 in the following $P_{X,plat}$ phases, respectively. The duration of the $P_{X,plat}$ is estimated to be ∼58 days for the second $P_{X,plat}$ and ∼54 days for the third $P_{X,plat}$, implying that the duration of the $P_{X,plat}$ phase does not change significantly. A dip for lessthanabouttwo weeks can also be seen in the X-ray band in both the second and third $P_{X,plat}$ phases. The $f_{X,soft}$ dropped by a factor of ∼2 during the two X-ray dips.

The UV showed very different variability during the second and third $P_{X,plat}$ phases. In the second $P_{X,plat}$ phase, a decline in the UV brightness is clearly seen in the *Swift*/UVM2 light curves, with an indication of a short UV plateau phase at the beginning of the $P_{X,plat}$. In contrast, the overall UV brightness does not vary significantly during the third $P_{X,plat}$ phase, with evidence of short-term variability on a timescale of aboutone week.

We carried out two radio observations during the third $P_{X,plat}$ phase. J0456−20 was detected in both radio observations. The flux densities of J0456−20 during the first observation measured at 5, 6, and 9 GHz are 257 ± 11, 278 ± 11, and 311 ± 12 μJy (Fig. 3), respectively. For the second radio observation, which was performed ∼16 days after the first, the source was detected in the 5.5, 9, and 17 GHz with flux density of 61 ± 18, 103 ± 23, and 117 ± 22 μJy (Fig. 3), respectively. We measured a 3σ upper limit of 738(198) μJy at the 2.1(22) GHz band. Our results suggest that the radio emission during the two detections declined rapidly; the flux density decreased by a factor of ∼3(4) in abouttwo weeks in the 9(5.5) GHz band (see Fig. 3). Overall, the radio flux density at 9(5.5) GHz increased by factors of ≳5(3), 6(7), and 5(2) compared to that in the $P_{X,drop}$, $P_{X,faint}$, and $P_{X,rise}$ phase, respectively.

3.2. Short-term X-ray temporal variability

The *XMM-Newton* pn 0.2−2.0 keV light curves for X2, X3, and X4 (Fig. 4) exhibit significant short-term variability with an
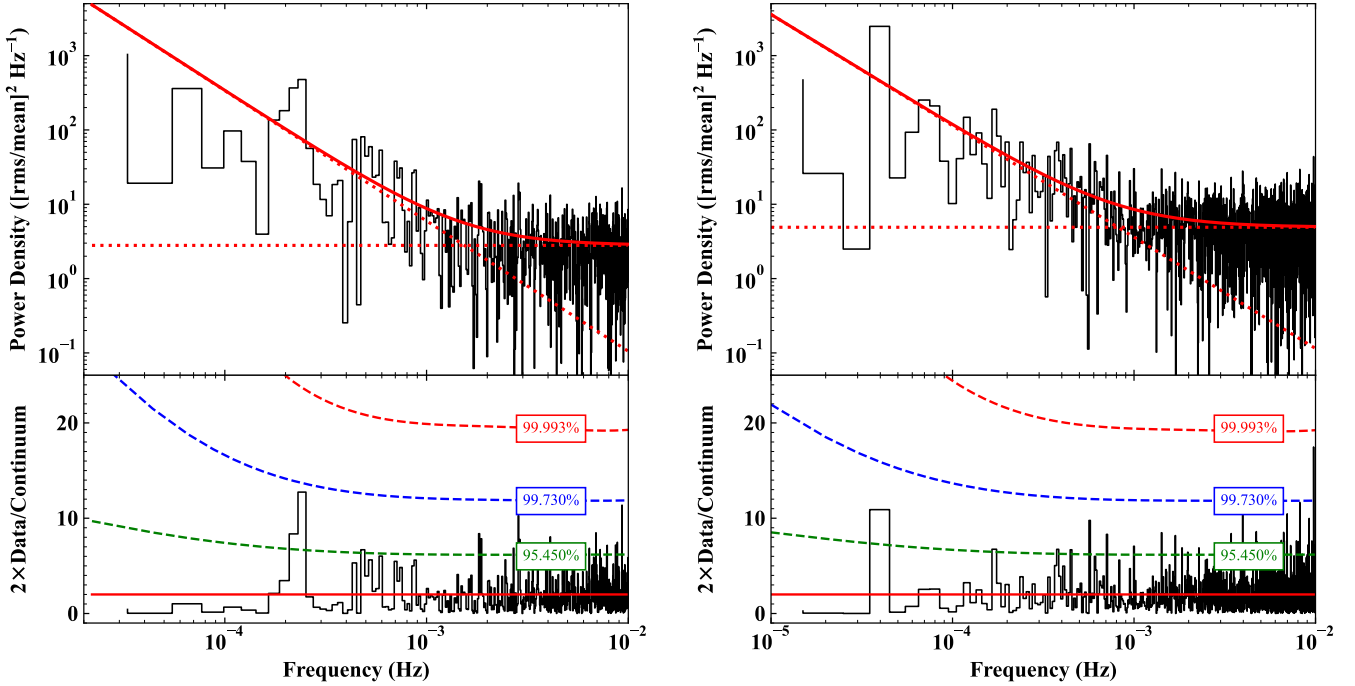
Fig. 5. PSDs for X2 and X3. *Left panel:* PSD calculated using the pn light curve of X2 in the 0.3−0.8 keV energy range with time bin-size of 50 s (upper panel). The solid red line indicates the best-fitting power-law plus Poisson constant model. The dotted red line shows the power-law component. The bottom panel shows the ratio of the data to the model multiplied by 2. This ratio roughly indicates the significance of the deviation of the observed power from the model continuum at a given frequency. The 2, 3, and 4σ confidence levels are marked with dashed green, blue, and red lines, respectively. *Right panel:* Same as the left panel, but for X3. A peak at a frequency of 2.5×10^{-4} Hz is seen in the PSD of X2 with a significance of $\sim 2.9\sigma$.

amplitude larger than a factor of 2 on a timescale of hours during all three *XMM-Newton* observations. We performed a timing analysis in the frequency domain in order to better characterise the broadband variability properties, characterise the putative repeating signal implied by the light curve (henceforth referred to as a quasi-periodic oscillation, or QPO), and to deconvolve a putative QPO from stochastic, broadband red-noise variability. We calculated the power spectral densities (PSDs) for X2 and X3 in the very soft 0.3−0.8 keV energy band. The first 1750 s data from X2 were excluded because of the large gap in the light curve. Only the first 100 ks data of X3 were used as the remaining 27 ks were severely affected by high-background flaring.

The calculated PSDs from X2 and X3 are shown in the left and right panels of Fig. 5, respectively. The PSDs were normalised so that the integrated PSD represents the fractional rms variability (e.g. Belloni & Hasinger 1990). We found an indication of a tentative QPO signal in the PSDs of X2.

However, stochastic red-noise processes will generate power in the PSD across a wide band of frequencies. These processes can spuriously mimic a few-cycle QPO, particularly in the low-frequency regime of the periodogram, where data sampling can be relatively sparse (Vaughan et al. 2016). We thus emphasise that because of the low temporal frequency of the QPO and the very small number of cycles sampled, any claim of a QPO (any claim that we have successfully deconvolved red noise from a QPO signal) is tentative at best. To assess the significance of the QPO, we first modelled the PSDs and then ran a Markov chain Monte Carlo (MCMC) code to estimate the confidence level of the QPO. The PSDs were fit with a power-law continuum model, adding a constant component to account for the Poisson white noise. The maximum likelihood estimate (MLE) method (Vaughan 2010) was used to estimate the model parameters. We

found a best-fitting power-law index of 1.75 ± 0.22 (1.50 ± 0.18) for X2 (X3). A QPO-like signal at frequency of 2.5×10^{-4} Hz is shown in the ratio of the data to model times 2 ($2R_{\text{PSD}}$, bottom panel in Fig. 5). This ratio roughly indicates the significance of the deviation of the observed power from the model continuum at a given frequency (Vaughan 2010).

To calculate the significance of the signal, we first simulated the continuum model using the initial values of the MLE parameters, assuming a uniform prior probability density function (Vaughan 2010). The PYTHON `emcee` package was used to perform MCMC sampling in order to draw from the posterior of model parameters. We generated 10^5 posterior predictive periodograms and simulated light curves for each of them using the method presented in Timmer & Koenig (1995). The MLE method was then applied to fit the simulated light curves using the same power-law plus white-noise model, and the $2R_{\text{PSD}}$ was calculated for each of the 10^5 simulated light curves. The 2, 3, and 4σ confidence levels were then estimated by calculating the 95.45, 99.73, and 99.993 percentiles of the $2R_{\text{PSD}}$ at each frequency bin (see the dashed lines in the bottom panel of Fig. 5). Our results suggest that a signal at a frequency of 2.5×10^{-4} Hz is tentatively detected at a 2.9σ level in X2, but no significant signal is found in X3.

3.3. X-ray spectral analysis

The XSPEC software (version `12.12.0a`; Arnaud 1996) was used to fit all X-ray spectra. The *Swift*/XRT X-ray spectra have low photon counts, thus the Cash statistic (Cash 1979, Cstat in XSPEC) is used. The χ^2 statistic is used for *XMM-Newton* and nicer spectral fitting. The XSPEC models TBabs and zTBabs (Wilms et al. 2000, abundances were set to `wilms` in XSPEC)
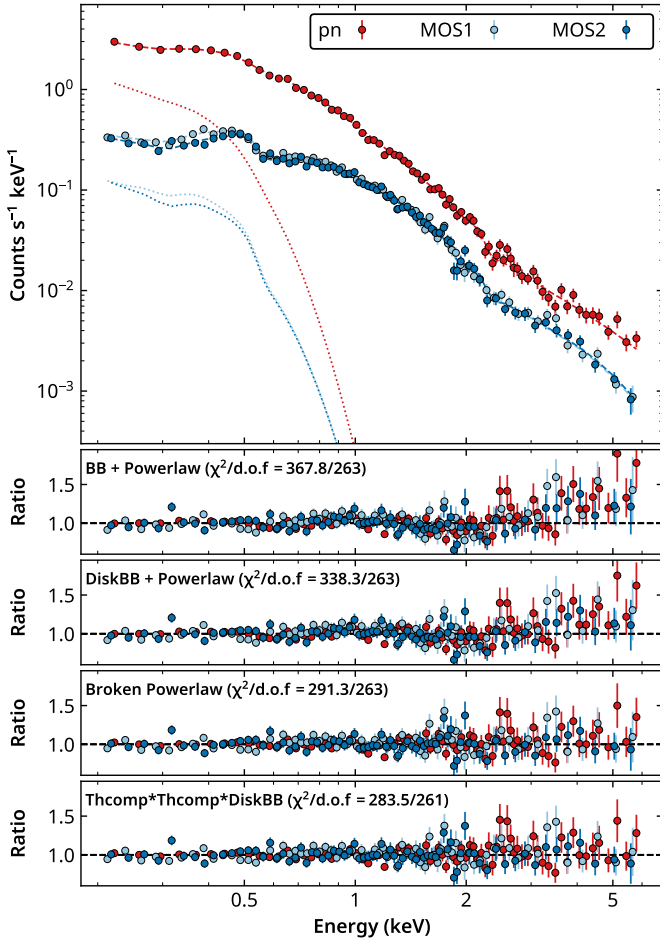
Fig. 6. X-ray spectral modelling. Upper panel: X-ray spectra of J0456−20 using the data from X2, with EPIC/pn shown in red, EPIC/MOS1 in dark blue, and EPIC/MOS2 in light blue. The best-fitting Comptonisation model ($M_{\rm comp}$) is shown as dashed lines, and the dotted lines represent the `diskbb` component in the $M_{\rm comp}$ model. Bottom panels: Data/model ratio for the $M_{\rm pbb}$, $M_{\rm pdb}$, $M_{\rm bkp}$, and $M_{\rm comp}$ models (from top to bottom).

were used to model the Galactic and host galaxy absorption, respectively.

3.3.1. Modelling time-averaged *XMM-Newton* data

The three *XMM-Newton* observations (X2, X3, and X4) provide the best S/N for X-ray spectral modelling. The data above 6.0 keV are dominated by background; we thus fitted the data from the three EPIC cameras (pn, MOS1, and MOS2) simultaneously over the 0.2−6.0 keV energy range. A constant component was added to account for the flux calibration difference between the three cameras.

We first fitted each of the time-averaged data of the three *XMM-Newton* observations (i.e. X2, X3, and X4) with a simple power-law model modified by both Galactic and host galaxy absorption (i.e. `const*TBabs*zTBabs*cflux*powerlaw` in XSPEC). No strong evidence for significant host galaxy absorption is found in each data set. We thus removed the host galaxy absorption component from our spectral modelling (the $M_{\rm pl}$ model, i.e. `const*TBabs*cflux*powerlaw`). The simple power-law model cannot fit the X-ray spectra of X2 well with χ^2/d.o.f. = 569.8/265. The fit can be signifi-

cantly improved by adding a blackbody component, that is, `const*TBabs*zashift*(cflux*powerlaw+cflux*bbody)` (hereafter $M_{\rm pbb}$), which gives a χ^2/d.o.f. of 367.8/263. The spectral fitting can be further improved by replacing the blackbody component with a multi-colour disk component, that is, `const*TBabs*zashift*(cflux*powerlaw+cflux*diskbb)` (hereafter $M_{\rm pdb}$), which gives a χ^2/d.o.f. of 338.3/263.

The same models were also used to fit the X3 and X4 data. We again found that the $M_{\rm pl}$ model cannot fit the X3 and X4 data well with χ^2/d.o.f. of 577.3/289 and 177.9/147, respectively. We obtained acceptable fits for X4 with both the $M_{\rm pbb}$ (χ^2/d.o.f. = 145.1/145) and $M_{\rm pdb}$ (χ^2/d.o.f. = 144.7/145) models. Similar to X2, the $M_{\rm pdb}$ model, which gives a χ^2/d.o.f. of 333.3/287, can fit the X3 spectra better than the $M_{\rm pbb}$ model (χ^2/d.o.f. = 367.0/287). However, systematical features at energies above 3 keV are clearly seen in the residuals for both X2 and X3 (see Fig. 6). The details of the spectral fitting are listed in Table 4.

The excesses at higher energy for X2 and X3 suggests the need for an additional spectral component. We then tried to fit the data with a broken power-law model (`const*TBabs*(cflux*bknpower)`, hereafter $M_{\rm bkp}$). The $M_{\rm bkp}$ model can fit both the X2 and X3 spectra well with χ^2/d.o.f. of 291.3/263 and 287.6/287, respectively. The best-fitting break energy for X2 is $1.86^{+0.18}_{-0.14}$ keV with $\Gamma_1 = 3.43 \pm 0.03$ and $\Gamma_2 = 2.54^{+0.11}_{-0.13}$. We obtained a shallower Γ_1 (3.31 ± 0.03) for X3, while the best-fitting $E_{\rm Br} = 1.93^{+0.16}_{-0.13}$ and $\Gamma_2 = 2.46^{+0.10}_{-0.12}$ are consistent within their uncertainties with X2. The $M_{\rm bkp}$ model can also fit the X4 data well. The best-fitting parameters for X4 are consistent with those from X2 and X3. Overall, the $M_{\rm bkp}$ model is preferred over the $M_{\rm pbb}$ and $M_{\rm pdb}$ models for both X2 and X3, while all the three models give acceptable fits for X4. In Table 4 we list the best-fitting parameters of the $M_{\rm bkp}$ model for the three observations.

The broken power-law fitting may be an indication that there are two coronae in J0456−20. The power-law component in the soft X-ray band could be due to inverse Comptonisation of the soft accretion disk photons by a warm corona with an electron temperature of a few keV or lower, and a hot corona may contribute to the hard-band power law. We then fit the X2 and X3 data with a model consisting of two inverse Comptonisation components, `const*TBabs*zashift*(cflux*thcomp*thcomp*diskbb)` ($M_{\rm comp}$). This model was used to fit the X-ray spectra of bright AGNs (e.g. Jin et al. 2021). To better constrain the temperature of the multi-colour component, which may well peak in the UV band, we fitted the 0.2−6.0 keV X-ray data along with the OM/UVM2 data. The Galactic dust reddening is estimated to be $E_{B-V} = 0.03$ mag using the dust map (Schlafly & Finkbeiner 2011). The electron temperature of the hot corona cannot be constrained and was therefore fixed at 150 keV. Overall, the best-fitting parameters for the two time-averaged spectra are consistent with each other. We found that a low electron temperature is required for the warm corona components for both X2 ($kT_{\rm e} = 0.25^{+0.10}_{-0.07}$ keV) and X3 ($kT_{\rm e} = 0.27^{+0.06}_{-0.07}$ keV). The covering factor of the hot corona is small ($\rm CF_{hot} = 0.14^{+0.06}_{-0.05}$) in both cases, and only a lower limit can be given for the warm corona ($\rm CF_{warm} > 0.23$ for X2, and >0.32 for X3). The inner temperature of the multi-colour disk is constrained to be ≈ 60 eV for both data with $T_{\rm in} = 64^{+13}_{-10}$ eV for X2 and 61^{+21}_{-7} eV for X3. The details of the best-fitting parameters and the uncertainties are listed in Table 4. The results suggest that the time-averaged X-ray spectral properties do not evolve significantly over a timescale of several months.

Table 4. Results of the X-ray spectral fitting.

			$M_{\rm bkp}$ `const*TBabs*(cflux*bknpower)`			
Parameters	$N_{\rm H,Gal}$ $(10^{20}\,{\rm cm}^{-2})$	Γ_1	$E_{\rm Br}$ (keV)	Γ_2	$\log f_{\rm soft}$ $({\rm erg\,cm}^{-2}\,{\rm s}^{-1})$	χ^2/d.o.f.
X2	4.4 ± 0.2	3.43 ± 0.03	$1.86^{+0.18}_{-0.14}$	$2.54^{+0.11}_{-0.13}$	-11.21 ± 0.02	291.3/263
X3	5.1 ± 0.3	3.31 ± 0.03	$1.93^{+0.16}_{-0.13}$	$2.46^{+0.10}_{-0.12}$	-11.49 ± 0.02	287.6/287
X4	$5.4^{+0.8}_{-0.6}$	$3.33^{+0.10}_{-0.07}$	$1.72^{+0.37}_{-0.15}$	$2.61^{+0.20}_{-0.18}$	-11.61 ± 0.04	141.7/145
X2-LO	4.6 ± 0.2	$3.35^{+0.04}_{-0.03}$	$2.23^{+0.20}_{-0.27}$	$2.30^{+0.22}_{-0.20}$	-11.30 ± 0.02	444.3/412
X2-HI		3.52 ± 0.04	$1.72^{+0.12}_{-0.11}$	$2.60^{+0.10}_{-0.11}$	-11.12 ± 0.02	

			$M_{\rm pbb}$ `const*TBabs*zashift*(cflux*powerlaw+cflux*bbody)`				
Parameters	$N_{\rm H,Gal}$ $(10^{20}\,{\rm cm}^{-2})$	kT (eV)	Γ	$\log f_{\rm soft,bb}$ $({\rm erg\,cm}^{-2}\,{\rm s}^{-1})$	$\log f_{\rm soft,po}$ $({\rm erg\,cm}^{-2}\,{\rm s}^{-1})$	$\log f_{\rm soft}$ $({\rm erg\,cm}^{-2}\,{\rm s}^{-1})$	χ^2/d.o.f.
X2	2.3 ± 0.3	108 ± 4	2.86 ± 0.05	-12.03 ± 0.04	-11.54 ± 0.03	-11.42 ± 0.03	367.8/263
X3	2.5 ± 0.3	119 ± 4	2.75 ± 0.05	-12.35 ± 0.04	-11.82 ± 0.03	-11.71 ± 0.03	367.0/287
X4	2.3 ± 0.8	128^{+9}_{-10}	2.74 ± 0.13	$-12.50^{+0.08}_{-0.12}$	-11.97 ± 0.09	-11.86 ± 0.07	145.1/145
X2-LO	2.3 ± 0.3	117 ± 5	2.84 ± 0.07	$-12.18^{+0.06}_{-0.08}$	-11.62 ± 0.04	-11.51 ± 0.04	519.9/412
X2-HI		105 ± 4	2.86 ± 0.06	$-11.91^{+0.04}_{-0.05}$	-11.50 ± 0.04	-11.35 ± 0.03	

			$M_{\rm pdb}$ `const*TBabs*zashift*(cflux*powerlaw+cflux*diskbb)`				
Parameters	$N_{\rm H,Gal}$ $(10^{20}\,{\rm cm}^{-2})$	$T_{\rm in}$ (eV)	Γ	$\log f_{\rm soft,diskbb}$ $({\rm erg\,cm}^{-2}\,{\rm s}^{-1})$	$\log f_{\rm soft,po}$ $({\rm erg\,cm}^{-2}\,{\rm s}^{-1})$	$\log f_{\rm soft}$ $({\rm erg\,cm}^{-2}\,{\rm s}^{-1})$	χ^2/d.o.f.
X2	2.4 ± 0.3	$144\pm^{+5}_{-6}$	2.76 ± 0.06	$-11.85^{+0.03}_{-0.04}$	-11.61 ± 0.04	-11.41 ± 0.03	338.3/263
X3	2.6 ± 0.3	160 ± 6	2.64 ± 0.06	$-12.15^{+0.03}_{-0.04}$	-11.89 ± 0.03	-11.70 ± 0.03	333.3/287
X4	$2.5^{+0.8}_{-0.7}$	171^{+14}_{-15}	2.64 ± 0.16	$-12.30^{+0.07}_{-0.11}$	-12.05 ± 0.11	-11.86 ± 0.08	144.7/145
X2-LO	2.4 ± 0.3	154^{+7}_{-8}	2.75 ± 0.09	$-11.98^{+0.06}_{-0.07}$	-11.68 ± 0.06	-11.51 ± 0.04	491.8/412
X2-HI		139 ± 6	2.77 ± 0.07	-11.74 ± 0.04	-11.57 ± 0.05	-11.34 ± 0.03	

			$M_{\rm comp}$ `const*TBabs*zashift*(cflux*thcomp*thcomp*diskbb)`						
Parameters	$N_{\rm H,Gal}$ $(10^{20}\,{\rm cm}^{-2})$	$T_{\rm in}$ (eV)	$\Gamma_{\rm hot}$	${\rm CF}_{\rm hot}$	$\Gamma_{\rm warm}$	$kT_{\rm e}$ (keV)	${\rm CF}_{\rm warm}$	$\log f_{\rm soft}$ $({\rm erg\,cm}^{-2}\,{\rm s}^{-1})$	χ^2/d.o.f.
X2	3.5 ± 0.4	64^{+13}_{-10}	$2.40^{+0.14}_{-0.18}$	$0.14^{+0.06}_{-0.05}$	$3.04^{+0.36}_{-0.85}$	$0.25^{+0.10}_{-0.07}$	≥ 0.23	-11.32 ± 0.09	283.5/261
X3	$3.8^{+0.5}_{-0.4}$	61^{+21}_{-7}	$2.29^{+0.13}_{-0.14}$	$0.14^{+0.06}_{-0.05}$	$2.97^{+0.15}_{-0.65}$	$0.27^{+0.06}_{-0.07}$	≥ 0.30	$-11.62^{+0.12}_{-0.07}$	280.0/285

Notes. $N_{\rm H,Gal}$ is the column density of the Galactic absorption; $E_{\rm Br}$ is the break energy in the `bknpower` component; Γ_1 and Γ_2 are the photon indices at lower and higher energies compared to $E_{\rm Br}$, respectively; kT is the temperature in the `bbody` model; $T_{\rm in}$ is the temperature of the inner region of the accretion disk in the `diskbb` model; Γ is the photon index in the `powerlaw` model; $\Gamma_{\rm hot}$ and ${\rm CF}_{\rm hot}$ are the power-law photon index and covering fraction for the hot corona, respectively, modelled with the `thcomp` model; $\Gamma_{\rm warm}$ and ${\rm CF}_{\rm warm}$ are for the warm corona; $kT_{\rm e}$ is the electron temperature of the warm corona; $f_{\rm soft,diskbb}$, $f_{\rm soft,bb}$, $f_{\rm soft,po}$ are the intrinsic flux calculated over the rest-frame 0.2−2.0 keV band for the `diskbb`, `bbody`, and `powerlaw` model, respectively; $f_{\rm soft}$ is the total intrinsic 0.2−2.0 keV flux. X2 was taken at the end of the $P_{\rm X,rise}$ phase. X3 and X4 were taken during the $P_{\rm X,plat}$ phase.

3.3.2. Short-term X-ray spectral variability

Figure 4 shows significant X-ray variability in J0456−20 on timescales as short as a few hours during the X2 and X3 observations. To test whether the X-ray spectral properties evolved on short timescales, we split the X2 event lists into two segments. As shown in Fig. 4, the source was in a relatively low X-ray flux state in the first segment (X2-LO), while the overall X-ray flux is higher in the second segment (X2-HI). The same models were used to fit the X-ray spectra extracted from the two segments. We found that the temperature of the blackbody (multi-colour disk) is slightly lower in the high flux state when it is fitted with the $M_{\rm pbb}$ ($M_{\rm pdb}$) model (see Table 4). The photon index in the soft X-ray band changed significantly in the two flux states when fitted with the $M_{\rm bkp}$ model. This is clearly illustrated in Fig. 7, in which we show the $\Delta\chi^2$ contours for the photon index in the soft X-ray band and the break energy in the $M_{\rm bkp}$ model. Our spectral analysis suggests that J0456−20 shows rapid X-ray spectral evolution on a timescale of a few hours.

3.3.3. Long-term X-ray spectral evolution

J0456−20 showed dramatic long-term X-ray variability with four distinctive phases. It is interesting to probe whether a spectral evolution occurred when the source transitioned between different flux levels. The S/N of most of the available X-ray data is low. Thus, we fitted the *Swift*/XRT (except for the one at around MJD 59391, hereafter Swift5), NICER, and eROSITA eRASS3/4 spectra with the simple power-law model ($M_{\rm pl}$). We also fixed $N_{\rm H,Gal}$ at 3.3×10^{20} cm^{-2} (Willingale et al. 2013). The distribution of the best-fitting photon index is shown in the upper panel of Fig. 8 (the definition of the three cycles is given in Sect. 4). It is evident that the spectra are very soft at low fluxes (or at the $P_{\rm X,rise}$ phase, $\Gamma \gtrsim 3.0$) and become harder as the X-ray flux increases ($\Gamma \lesssim 3.0$), although the uncertainties are large.

The X-ray spectra during the faintest observed X-ray flux (i.e. in eRASS2, X1, and Swift5) are very soft and essentially lack source photons above 0.6 keV in the Swift5 XRT data and 1.0 keV in the eRASS2 and X1 data. We thus fitted each of the eRASS2, X1, and Swift5 spectra with
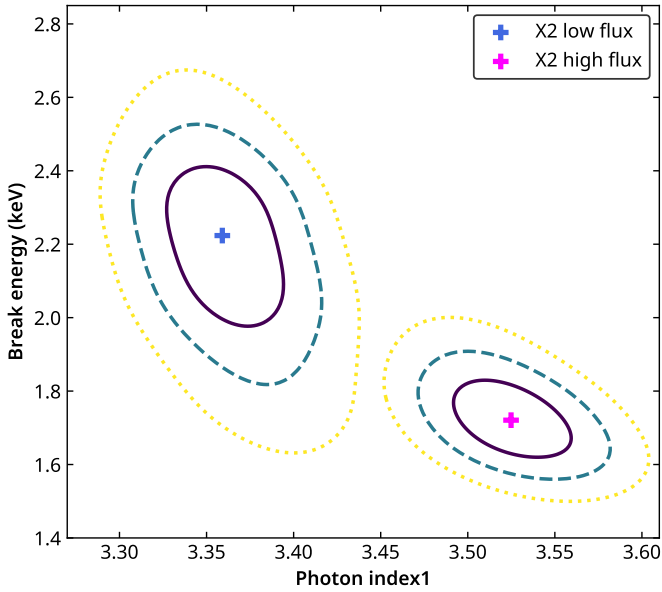
Fig. 7. Contours of the photon index vs break energy for X2-LO and X2-HI; solid, dashed, and dotted lines denote 1 ($\Delta\chi^2 = 2.3$), 2 ($\Delta\chi^2 = 6.18$), and 3σ ($\Delta\chi^2 = 11.83$) confidence contours, respectively.

a multi-colour disk model modified by Galactic absorption (TBabs*zashift*cflux*diskbb, hereafter $M_{\rm mcd}$) and fixed the Galactic column density at 3.3×10^{20} cm^{-2}. We obtained a best-fitting inner disk temperature $T_{\rm in}$ of 64^{+29}_{-18} eV with $f_{\rm X,soft}$ of $5.1^{+5.1}_{-2.6} \times 10^{-13}$ erg cm^{-2} s^{-1} for eRASS2. The value of $T_{\rm in}$ cannot be constrained by the *Swift*/XRT data with only a lower limit of 29 eV. We thus fixed it at its best-fitting value of 78 eV. This resulted in a $f_{\rm X,soft}$ of $1.8^{+1.8}_{-1.1} \times 10^{-13}$ erg cm^{-2} s^{-1}. For X1, we obtained a best-fitting inner disk temperature of 99^{+120}_{-40} eV and $f_{\rm X,soft}$ of $2.9^{+6.0}_{-1.8} \times 10^{-14}$ erg cm^{-2} s^{-1}.

3.4. Black hole mass estimation

We used two independent observed empirical relations, the $M_{\rm BH} - \sigma_\star$ relation (Ferrarese & Merritt 2000; Gebhardt et al. 2000) and the $M_{\rm BH} - \sigma^2_{\rm rms}$ relation (Ponti et al. 2012; $\sigma^2_{\rm rms}$ is the normalised excess variance, see below for more details), to estimate the mass of the central BH in J0456−20.

3.4.1. $M_{\rm BH}$ measured from the $M_{\rm BH} - \sigma_\star$ relation

The Magellan LDSS3-C spectrum was used as it provides the best balance between wavelength coverage and S/N. Using the spectral lamp, we measured an instrument FWHM of 4.6 pixels across the LDSS3-C band coverage. When the instrumental dispersion (2 Å per pixel) is taken into account, this resulted in an instrumental FWHM of ~9 Å, corresponding to an instrumental velocity resolution of ~208, 181, and 125 km s^{-1} at observed wavelengths of 5500, 6340, and 9200 Å, respectively. We adopted the pPXF package, a Python implementation of the penalised pixel-fitting method (Cappellari 2017), to measure the stellar velocity dispersion $\sigma_\star$. The Indo-US Library of Coudé Feed Stellar Spectra Library, consisting of 1237 stars covering the region of 3460−9464 Å (Valdes et al. 2004), was used to construct stellar templates to fit the Magellan spectrum. We created 1000 spectral realisations by resampling the Magellan data within the uncertainties, and performed pPXF fitting over
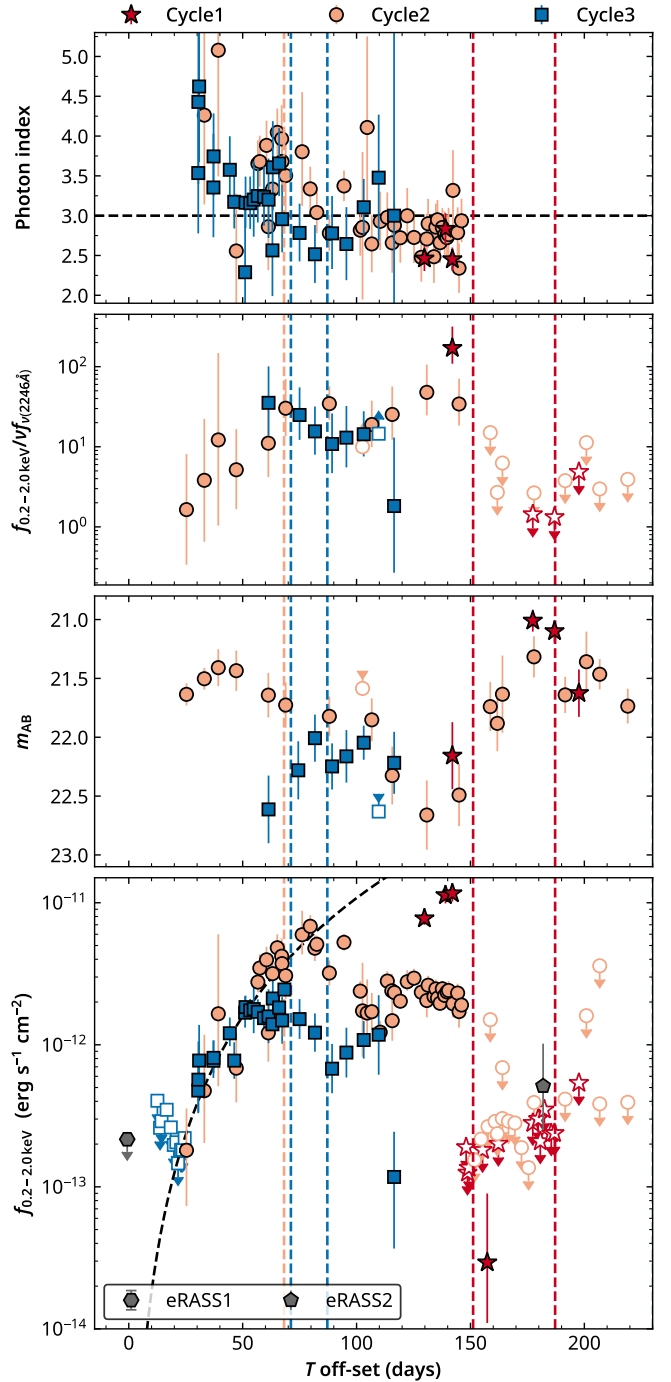

Fig. 8. From top to bottom: evolution of the photon index (measured using the $M_{\rm pl}$ model), ratio of the $f_{0.2-2.0\,\rm keV}$ to the 2246Å monochromatic flux, apparent UVM2 AB magnitude, and $\log(f_{0.2-2.0\,\rm keV})$ against the time offset. The time off-set is calculated relative to the inferred t_0 assuming a period of 223 days. The whole data set was split into three cycles that were determined by the time when the rapid X-ray flux drop occurred. The vertical dashed lines represent the time (relative to t_0 of each cycle) of the ATCA radio observations. Radio emission was detected only in cycle 3 (dashed blue lines).

the rest-frame 3900−8700 Å range for each of the realisations. The mean (140 km s^{-1}) and standard deviation (34 km s^{-1}) of the best-fitting values of $\sigma_\star$ are reported here as the intrinsic velocity dispersion and the 1σ uncertainty, respectively. This results in a BH mass of $\log(M_{\rm BH}/M_\odot) = 7.4 \pm 0.5$ using the relation

reported in Gültekin et al. (2009). The WiFeS data have a better spectral resolution ($\sim$1.7 Å, $\sigma_{\rm inst} \sim 50\,{\rm km\,s^{-1}}$) than the Magellan data, although their S/N is lower. We again performed pPXF fitting over the blue band (3900−5900 Å) of 1000 spectral realisations generated by resampling the WiFeS data. We measured a velocity dispersion of $120\pm20\,{\rm km\,s^{-1}}$, which leads to a BH mass of $\log(M_{\rm BH}/M_\odot) = 7.0 \pm 0.4$. This value is consistent with the value measured from Magellan data.

3.4.2. $M_{\rm BH}$ measured from $\sigma^2_{\rm rms} - M_{\rm BH}$ relation

A strong correlation between the $M_{\rm BH}$ and the normalised excess variance $\sigma^2_{\rm rms}$ has been reported for AGNs (Ponti et al. 2012; Pan et al. 2015). We also estimated the $M_{\rm BH}$ of J0456−20 using this empirical correlation, assuming that its short-term X-ray variability is similar to that of AGNs. The $\sigma^2_{\rm rms}$ was calculated using the following formula (e.g. Nandra et al. 1997):

$$\sigma^2_{\rm rms} = \frac{1}{N\mu^2} \sum_{i=1}^{N} [(X_i - \mu)^2 - \sigma_i^2],$$

where N is the number of bins in the X-ray light curve, and μ is the unweighted arithmetic mean of the photon count rates of the light curve. X_i and σ_i are the count rates and uncertainties in each time bin, respectively. The $\sigma^2_{\rm rms}$, however, depends on the time length, energy region, and time bin-size of the light curves. In this work, the $\sigma^2_{\rm rms}$ was calculated using the *XMM-Newton* EPIC/pn light curves over the 0.3−0.7 keV energy range with time bin-size of 250 s. To better estimate the uncertainty of the $\sigma^2_{\rm rms}$, we calculated $\sigma^2_{\rm rms}$ over 14 segments with 10 ks observation data of each using the X2 and X3 observations. We then estimated the $\log(\sigma^2_{\rm rms})$ and its 1σ uncertainty using the mean and standard deviation of the $\log(\sigma^2_{\rm rms})$ values calculated from the 14 segments, which give a $\log(\sigma^2_{\rm rms}) = -1.5 \pm 0.3$. We estimated a BH mass of $\log(M_{\rm BH}/M_\odot) = 6.4 \pm 0.2$ using the best-fitting model for a 10 ks segment presented in Ponti et al. (2012).

The value of $M_{\rm BH}$ measured from the $\sigma^2_{\rm rms} - M_{\rm BH}$ relation is lower than that from the $M_{\rm BH} - \sigma_\star$ relation. We note that the relation between $\sigma^2_{\rm rms}$ and $M_{\rm BH}$ was derived from a sample of persistently accreting AGNs with overall steady accretion flow. Thus, it does not necessarily apply to J0456−20, which may have a non-steady accretion disk. For instance, the $\sigma^2_{\rm rms}$ of the jetted TDE Swift 1644+57 shows a long-term evolution and can change by a factor of $\sim$5 in different flux states (Jin 2021). In this work, we assumed a BH mass of $10^7\,M_\odot$ for J0456−20. We note that the main conclusions of this paper do not change when a lower BH mass (e.g. $M_{\rm BH} = 3 \times 10^6\,M_\odot$, the mass measured from the $\sigma^2_{\rm rms} - M_{\rm BH}$ relation) is adopted.

4. Discussion

The long-term X-ray light curve of J0456−20 is characterised by four distinctive phases ($P_{\rm X,drop}$, $P_{\rm X,faint}$, $P_{\rm X,rise}$, and $P_{\rm X,plat}$). We define an X-ray variability cycle for J0456−20 as the time between the start of two consecutive $P_{\rm X,rise}$ phases (at the starting point of the dashed black and grey lines in the upper panel Fig. 1). We therefore observed three cycles (MJD before 59377 for cycle1, MJD after 59598 for cycle3, and the MJD in between for cycle2), and each of the four phases was observed at least twice (see Fig. 1). We derived a start time of MJD 59366 for cycle2 from the best-fitting t_0 of the second $P_{\rm X,rise}$ (see Sect. 3.1). The start times for cycle1 and cycle3 were then estimated by assuming a recurrence time of 223 days. Figure 8 shows the X-ray flux against the time offset for the 3 cycles, where the time

offsets were calculated with respect to the start time for each cycle. The profile of the first $P_{\rm X,rise}$ phase is well described by a power-law function (Fig. 1 and bottom panel of Fig. 8). Remarkably, the same function can also match the profile of the second $P_{\rm X,rise}$ phase well. The characteristic of the long-term X-ray light curve strongly suggests that J0456−20 is a repeating, or even periodic, X-ray nuclear transient with a roughly estimated recurrence time of 223 days. This adds a member to this rare class of nuclear transients. We further note that, unlike ASASSN-14ko and IC 3599, no strong broad or narrow emission lines (e.g. the [O III]λ4959/5007 or the Balmer lines) are detected from our low- and medium-resolution optical spectroscopic data, indicating that the host galaxy of J0456−20 exhibited no signs of prior AGN activity.

4.1. Nature of J0456−20

Using the best-fitting $M_{\rm comp}$ models from X2 and X3 (see Sect. 3.3 and Table 4), which consist of a multi-colour disk and two Componization components, we can roughly estimate the bolometric luminosity from $L_{\rm X,soft}$ using a correction factor, $\kappa = L_{\rm bol}/L_{\rm X,soft}$, of $\sim$3. The peak values of $L_{\rm X,soft}$ are $\sim$1.6, 1.0, and $0.3 \times 10^{44}\,{\rm erg\,s^{-1}}$ (see Fig. 1) for cycle1, cycle2, and cycle3, respectively. Thus, when we assume a BH mass of $10^7\,M_\odot$, the observed peak Eddington ratios $\lambda_{\rm Edd} = L_{\rm bol}/L_{\rm Edd}$ in cycle1, cycle2, and cycle3, are $\sim$0.37, 0.23, and 0.07, respectively.

The total energy released in each cycle can be estimated by

$$E_{\rm tot} = L_{\rm fa}\Delta t_{\rm fa} + L_{\rm pl}\Delta t_{\rm pl} + \int_0^{\Delta t_{\rm rs}} L_{\rm rs}(t)\,{\rm d}t,$$

where $\Delta t_{\rm fa}$, $\Delta t_{\rm pl}$, and $\Delta t_{\rm rs}$ are the duration of the $P_{\rm X,faint}$, $P_{\rm X,plat}$, and $P_{\rm X,rise}$ phases, respectively. $L_{\rm fa}$ and $L_{\rm pl}$ are the average bolometric luminosity during the $P_{\rm X,faint}$ and $P_{\rm X,plat}$ phases, respectively, and we adopted the best-fitting power-law function of $f_{\rm rs}(t)$ found in cycle2 to describe the profile of $L_{\rm rs}(t) = \kappa_{\rm rs}4\pi D_{\rm ld}^2 f_{\rm rs}(t)$ for the $P_{\rm X,rise}$ phase for each of the three cycles. The bolometric correction factor, $\kappa_{\rm rs}$, could change from $\sim$20 at faint X-ray flux level to $\sim$3 at bright X-ray flux level (see Sect. 4.2) during the $P_{\rm X,rise}$ phase. We conservatively assumed an average value of 15 for $\kappa_{\rm rs}$. Using a bolometric correction factor of $\kappa = 3$, $L_{\rm pl}$ is estimated to be 4.8, 1.1, and $0.7 \times 10^{44}\,{\rm erg\,s^{-1}}$ for cycle1, cycle2, and cycle3, respectively. The values of $L_{\rm fa}$ are poorly constrained. We thus adopted a value of $9.0 \times 10^{43}\,{\rm erg\,s^{-1}}$, derived from Swift5 (see Sect. 4.2), for $L_{\rm fa}$ for each of the three cycles. The values of $\Delta t_{\rm fa}$, $\Delta t_{\rm rs}$ and $\Delta t_{\rm pl}$ are well constrained for cycle2 and cycle3 with $\Delta t_{\rm pl} = 2$ months and $\Delta t_{\rm fa} = 3$ months for both cycles, and $\Delta t_{\rm rs} = 3$ months for cycle2 and 2 months for cycle3. For cycle1, we assumed the values are 3, 4, and 2 months for $\Delta t_{\rm fa}$, $\Delta t_{\rm rs}$, and $\Delta t_{\rm pl}$, respectively. We then calculated a total released energy of $E_{\rm tot} = 1.5$, 0.5, and 0.2×10^{52} erg for cycle1, cycle2, and cycle3, respectively. When we assume that half of the tidally disrupted debris returns to the SMBH and that the radiation efficiency is 0.1, the total mass of the disrupted debris is about $0.17\,M_\odot$ for cycle1, $0.06\,M_\odot$ for cycle2, and $0.02\,M_\odot$ for cycle3.

4.1.1. Partial tidal disruption event

The very soft X-ray spectra in eRASS2 and at the beginning of the rising phase as well as the observed peak 0.2−2.0 keV luminosity of $\sim$1.6 $\times 10^{44}\,{\rm erg\,s^{-1}}$ are consistent with the expectation from a TDE. A pTDE is then required to produce the repeating X-ray flares seen in J0456−20. The estimated Eddington ratios
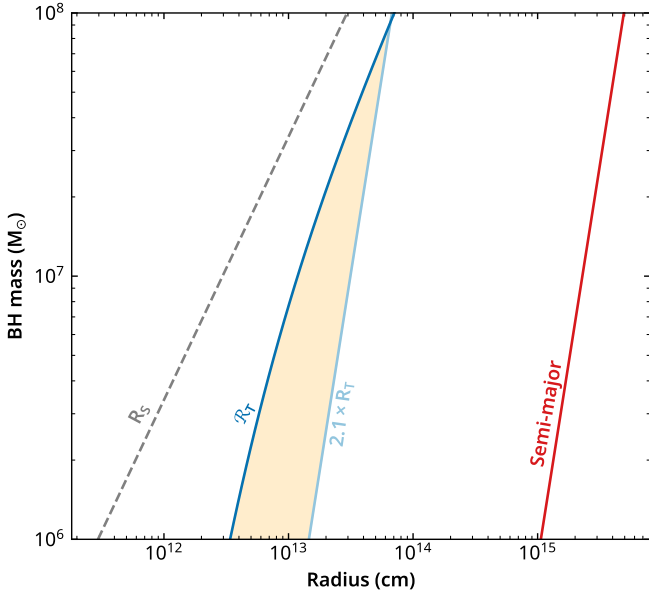
Fig. 9. Different radii as a function of BH mass. The Schwarzschild radius (R_S) is shown by the dashed grey line. The radius ($\mathcal{R}_T$) at which a full disruption of a solar-like main-sequence star would happen is marked by the solid blue line. The solid light blue line shows the tidal radius (R_T) multiplied by 2.1, which is roughly the radius at which a partial tidal disruption event would happen. The $2.1 \times R_T$ line also indicates the radius at which RLOF could happen. We show the semi-major axis for a period of 223 days in red.

are much lower than the Eddington accretion rate, but are reasonable for a pTDE (e.g. Guillochon & Ramirez-Ruiz 2013). The required mass loss for each cycle is also low enough for a repeating pTDE.

Figure 9 shows the characteristic radii for a main-sequence star with mass of $1\,M_\odot$ and radius of $1\,R_\odot$ as a function of $M_{\rm BH}$. The radius ($\mathcal{R}_T$) at which a full TDE will occur was calculated using the equation presented in Ryu et al. (2020a). The radius at which a pTDE can be expected to happen is approximately 2.1 times the tidal radius R_T (Ryu et al. 2020b). The orange shadowed region marks the parameter space where a pTDE can occur. Clearly, a pTDE is possible for J0456−20 even for a solar-type main-sequence star. The semi-major axis of the orbit of the star, assuming a period of 223 days, is also shown in Fig. 9. The semi-major axis is always at least ten times larger than $2.1\mathcal{R}_T$. A repeating pTDE with period of 223 days therefore remains a possible scenario for the origin J0456−20.

The orbital period of a star, which was fed to the SMBH through the traditional two-body scattering, can be estimated by $P \simeq \pi R_\star^{3/2}(M_{\rm BH}/M_\star)/\sqrt{2GM_\star}$ (Cufari et al. 2022), where $R_\star$ and $M_\star$ are the radius and mass of the star, respectively. For a solar-like star and $M_{\rm BH}$ of $10^7\,M_\odot$, the orbital period should be around 10^3 yr, which is much longer than the recurrence time of 223 days for J0456−20. Recently, Cufari et al. (2022, see also Amaro-Seoane et al. 2012) has proposed that the Hills mechanism, according to which a star in a binary system can be captured on a tightly bound orbit around the SMBH after the binary system is destroyed by the tides of the SMBH, can produce the short period (∼114 days) observed in ASASSN-14ko. With a semi-major axis $a_\star$ of the binary system of about 0.007 au[9], this mechanism can also generate the short period observed in

J0456−20. The tidal radius at which the Hills mechanism will take place can be calculated by $r_{\rm t} = a_\star(M_{\rm BH}/M_\star)^{1/3}$ (Hills 1988), which is about $15R_{\rm g}$ (∼2.3×10^{13} cm, $R_{\rm g} = GM_{\rm BH}/c^2$ is the gravitational radius) for J0456−20 assuming $a_\star = 0.007$ au. This also agrees with the radius required for a pTDE (Fig. 9).

The $P_{\rm X,drop}$ phase, however, is rarely seen in normal TDEs, which often show a decline in their X-ray light curve that is broadly consistent with the predicted $f \propto t^{-\beta}$ law with $\beta = 5/3$ (e.g. Komossa 2015; Saxton et al. 2021). It has been suggested that the fall-back rate of a pTDE can noticeably deviate from this relation. For instance, the slope calculated from hydrodynamic simulations in Guillochon & Ramirez-Ruiz (2013) can be as steep as $\beta > 3$. Coughlin & Nixon (2019) advocated that the asymptotic late-time fallback rate in a pTDE scales with $t^{-9/4}$. In the recent simulations by Ryu et al. (2020c), the decline in the fallback rate was argued to depend on the mass of the remnant, for instance, $\beta = 2$ for strong pTDE while $\beta = 5$ for a weak pTDE in a $10^6\,M_\odot$ BH. The slope of the X-ray light curve during the $P_{\rm X,drop}$ phase strongly depends on the time of the peak X-ray flux ($t_{\rm X,peak}$), which is unknown. We nevertheless estimated that β is larger than 8 using the Swift1 detection and the first NICER upper limit in the first $P_{\rm X,drop}$ phase, assuming that Swift1 was taken at least 10 days[10] after the $t_{\rm X,peak}$. It is thus unlikely that the rapid X-ray drop reflects a dramatic decrease in the fall-back rate. Rather, we interpret the X-ray flux drop as a transition of the accretion state (see Sect. 4.3 for more details).

Further evidence to support J0456−20 as a pTDE is the gradual decrease of the observed peak X-ray flux from cycle1 to cycle3. The same trend is also observed in the UV light curve, but it is less significant. This is consistent with the expectation from a pTDE, as less material is accreted onto the BH if the surviving star becomes more compact after each passage. However, we caution that, as pointed out by Ryu et al. (2020c), the stellar remnant could be expanded by additional heat and rotation, therefore a more severe pTDE is not impossible.

4.1.2. Other potential scenarios

Alternative scenarios, such as a superluminous supernova near the centre of the galaxy nucleus, can be ruled out as the X-ray luminosity evolution as well as the X-ray spectral properties of J0456−20 are very different from these events. Periodic flares can also be produced by collisions between consecutive EMRI that are in the process of stable mass-transfer via RLOF onto an SMBH (Metzger & Stone 2017). However, the recurrence time for this model is normally decades or even hundreds of years, which is much longer than the observed timescale for J0456−20. The predicted timescale can be significantly reduced, as short as hours, if the two stars reside in a common orbital plane (Metzger et al. 2022). This model has been proposed to explain the QPEs and the periodic flares observed in ASASSN-14ko. The BH mass estimated for J0456−20 is around $10^7\,M_\odot$, which is one order of magnitude lower than that in ASASSN-14ko. It is still possible to produce the observed recurrence timescale for J0456−20 as long as the stars have a much lower mean density (e.g. $\rho < 0.1\rho_\odot$). However, we note that the typical mass loss per collision from this model is in the order of $2 \times 10^{-4}\,M_\odot$ for $M_{\rm BH}$ of $10^7\,M_\odot$ and period of 223 days (equation 15 in Metzger et al. 2022), which is much lower than the estimated mass loss for J0456−20. We thus disfavour a pair of EMRIs as the cause for the repeating flares in this object.

---

[9] $P \simeq \pi a_\star^{3/2}(M_{\rm BH}/M_\star)^{1/2}/\sqrt{2GM_\star}$, Cufari et al. (2022)

[10] The $t_{\rm X,peak}$ is very likely before the first eRASS3 observation, which was taken ∼11 days before Swift1.

Disk instabilities, including the radiation pressure instability, have been proposed to explain the repeating rapid soft X-ray variability in the BHXRB GRS 1915+105 (Belloni et al. 1997) and also the soft X-ray flares in the galaxy IC 3599 (Grupe et al. 2015) and the AGN NGC 3599 (Saxton et al. 2015). In this scenario, in the X-ray faint state, the accretion disk (either from a pre-existing AGN or a newly formed disk after a TDE) is truncated at a certain radius R_{tr}. This truncated disk will be slowly refilled at a steady accretion rate from the outer disk. The time needed to refill the inner region (with inner radius of R_0) of the accretion disk is governed by the viscous timescale and can be estimated (Saxton et al. 2015) by

$$\tau_{fill} \sim 0.33\alpha^{-8/10}M_6^{6/5}m_{Edd}^{-3/10}\left[\left(\frac{R_{tr}}{R_g}\right)^{5/4} - \left(\frac{R_0}{R_g}\right)^{5/4}\right] \text{ months,}$$

where α is the viscosity parameter. M_6 is the BH mass in units of $10^6 M_\odot$ and R_g is the gravitational radius. m_{Edd} is the mass accretion rate in units of Eddington-limited accretion rate $\dot{M}_{Edd} = 1.4 \times 10^{18}(M_{BH}/M_\odot)$ g s^{-1}. Assuming a BH mass of $10^7 M_\odot$ with Eddington-limited accretion rate $m_{Edd} = 1$ and inner radius $R_0 = 3R_g$, we estimate the value of τ_{fill} to be $\gtrsim 56$ months even for a small truncation radius of $4 R_g$ with $\alpha = 0.1$, which is much longer than the observed duration ($\lesssim 3$ months) of the faint state for J0456$-$20. This timescale can be significantly shortened as in a toy model developed by Sniegowska et al. (2020; see also Pan et al. 2021), in which the radiation pressure instability only operates in a narrow ring between a thin outer disk and an optically thin hot inner ADAF. However, our X-ray spectral analysis suggests that the temperature of the inner-region of the multi-colour disk does not change at different X-ray flux states. This is inconsistent with the radiation instability, which predicts a hotter (cooler) disk at high (low) accretion rates. We thus also disfavour the disk instability as the cause for the repeating X-ray flares in J0456$-$20.

4.2. Mechanism for the X-ray and UV emission

The X2 and X3 observations provide high-quality data to understand the physical processes for the X-ray emission during the X-ray bright state (bright end of the $P_{X,rise}$ phase for X2 and $P_{X,plat}$ for X3). As mentioned in Sect. 3.3, the X-ray spectra of X2 and X3 can be best interpreted as inverse Comptonisation of the seed photons from a multi-colour thermal disk by the warm and hot coronae. The best-fitting temperature of the inner region T_{in} of the multi-colour disk is ~60 eV, suggesting that a thin thermal disk exists in the X-ray bright state. This thermal disk causes the UV emission and also contributes substantially to the very soft X-ray emission (<0.5 keV band), while the 0.5–2.0 keV X-ray emission is dominated by X-ray photons produced from the inverse Componisation by the two coronae.

The results of the X-ray spectral fitting are less certain in the faint state because the S/N is low. However, all three X-ray spectra observed during this state, that is, eRASS2, X1 (in the $P_{X,drop}$ phase), and Swift5 (at the beginning of the $P_{X,rise}$ phase), are very soft, suggesting that the X-ray emission may come from a thermal accretion disk with no indication of strong X-ray emission from the corona. The value of T_{in} is 67^{+29}_{-17} eV for eRASS2, ~78 eV for Swift5, and 99^{+120}_{-40} eV for X1 if fitted with a multi-colour accretion disk (the M_{mcd} model, see Sect. 3.3.3). We tested the emergence and potential evolution of a thermal accretion disk by modelling the broad-band UVOT/UVM2 and XRT/X-ray data of the five Swift observations (ObsIDs: 00014135005–00014135009), starting with Swift5, during the
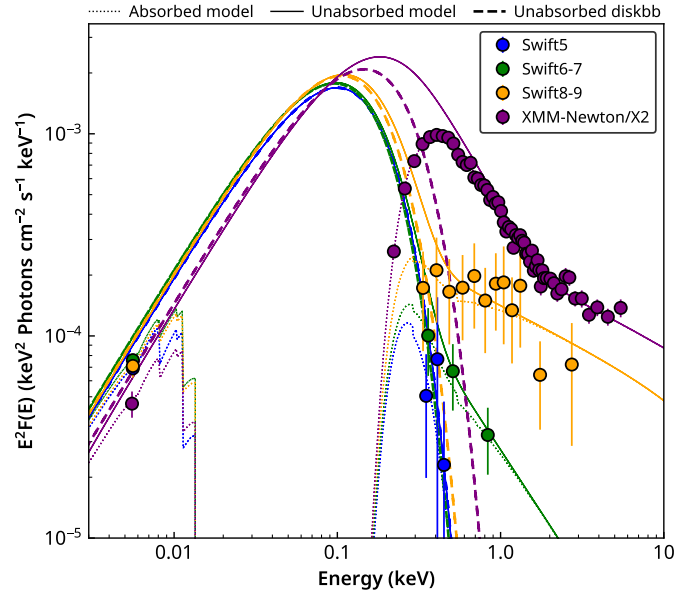

Fig. 10. Evolution of the UV/X-ray SED during the first $P_{X,rise}$ phase. The solid circles are the unfolded spectra for Swift5 (blue), Swift6-7 (green), Swift8-9 (orange), and *XMM-Newton*/X2 (purple). The dotted lines are the absorbed models. The solid and dashed lines represent the unabsorbed intrinsic model and the diskbb component, respectively.

first $P_{X,rise}$ phase (e.g. the dashed black line in the upper panel of Fig. 1). To increase the S/N, we stacked the observations 00014135006 and 00014135007, as well as 00014135008 and 00014135009, to two combined *Swift* observations (hereafter Swift6-7 and Swift 8-9). We then obtained the X-ray spectra and the UVM2 flux densities for each of the two combined *Swift* observations.

We first modelled the broad band UV and X-ray data with the M_{mcd} model for Swift5, Swift6-7, and Swift8-9. We again used $E_{B-V} = 0.03$ mag to correct the Galactic reddening. We note that due to the low photon counts, the XRT spectra follow Poisson distribution (fewer than ten counts per bin). While the UVOT/UVM2 data follow Gaussian statistics. Thus, the results from this spectral modelling should be treated with caution and should not be considered as the best-fitting model. Nevertheless, we found that the broad-band UV/X-ray data can be described with a single multi-colour disk model with a temperature of ~45 eV and L_{bol} of 9.0×10^{43} erg s^{-1} (6.0×10^{-12} erg cm^{-2} s^{-1}, $\lambda_{Edd} \approx 0.07$) for Swift5. The unfolded spectrum, M_{mcd} model, and absorption corrected intrinsic model are shown in Fig. 10. However, a simple M_{mcd} model cannot describe the X-ray data of Swift6-7 and Swift8-9 well, with clear excess above ~0.7 keV. Therefore, we added a Comptonisation component to the M_{mcd} model, that is, TBabs*zashift*(cflux*thcomp*diskbb) in XSPEC, to fit the Swift6-7 and Swift8-9 data. The electron temperature kT_e and the covering fraction cannot be constrained. We thus fixed kT_e at 10 keV and covering fraction at 0.01. As shown in Fig. 10, this model can indeed describe the broad band UV and X-ray data of both Swift6-7 and Swift8-9. The values of T_{in} are ~44 eV for Swift6-7 and ~48 eV for Swift8-9. For comparison, we also show the unfolded X2 data using the best-fitting M_{comp} model found in Sect. 3.3.1. We conclude that the UV and X-ray emission mainly originates from the thin thermal accretion disk in the faint state (illustrated in Fig. 11, sequence ②). As the $f_{X,soft}$ increases during the $P_{X,rise}$ phase, the warm and hot coronae start to form (sequence ③–④ in Fig. 11). X-ray photons
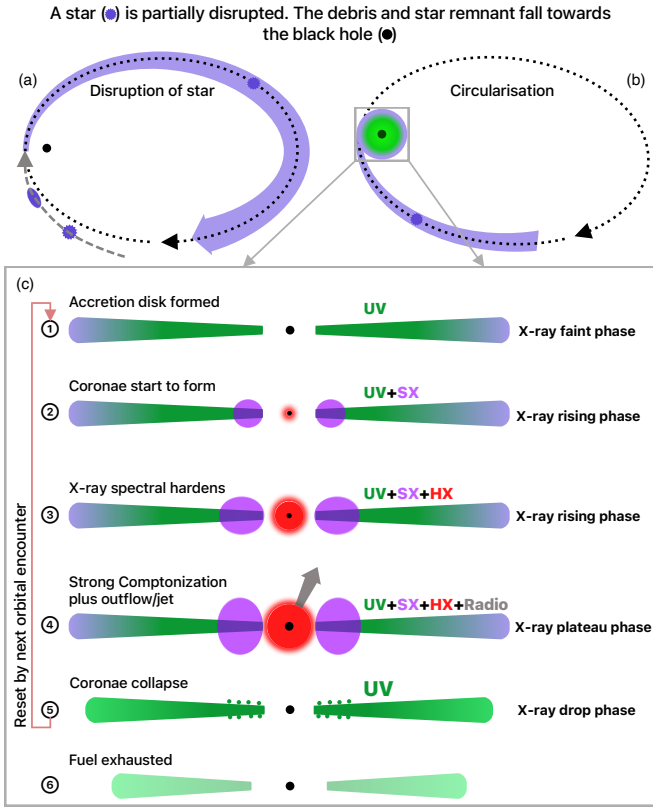
Fig. 11. Partially disrupted star upon pericentre passage around a BH (*panel a*). The initial orbit of the star is represented with a dashed grey curve. The dotted black curve represents the orbit of the stellar debris and remnant (panel a and b). The stellar debris is rapidly circularised, and an accretion disk is formed (*panel b*). The freed gas (blue) is accreted onto the BH, with the accretion process proceeding in phases ①–⑥ (*panel c*), with a sequential build-up ①–④ of an accretion disk (UV, green colour), warm (soft X-rays, purple) and hot corona (hard X-rays, red), as well as an outflow or jet (radio, grey). When the gas reservoir depletes, the corona collapses for unknown reasons (⑤, no X-ray emission), and the accretion of the remaining accretion disk gas is even more rapid, leading to enhanced UV emission. Finally, as the fuel is completely exhausted (6), the UV emission drops as well. However, the subsequent pericentre passage resets the cycle.

produced from the inverse Comptonisation of the two coronae start to dominate the X-ray emission.

Our results also indicate a rapid formation of the accretion disk, with a timescale comparable to the duration of $P_{X,faint}$ phase ($\lesssim 3$ months). For repeating pTDE, the stellar debris should be on an elliptical orbit. Hayasaki et al. (2013) showed in their simulations that an accretion disk can be formed rapidly for a star on an elliptical orbit with moderate eccentricity ($e = 0.8$) tidally disrupted by a $10^6 M_\odot$ SMBH with a deep encounter ($r_t/r_p = 5$, where r_p is the pericentre distance). The rapid circularisation is due to stellar stream collisions induced by relativistic apsidal precession. Relativistic precession has also been proposed to explain the rapid disk formation in TDE AT2018fyk (Wevers et al. 2019). For pTDE like J0456−20, a very deep encounter is unlikely. However, a moderate encounter with $r_t/r_p < 2$ is still possible for more centrally concentrated stars (Guillochon & Ramirez-Ruiz 2013; Ryu et al. 2020c). Combined with a higher BH mass of $10^7 M_{BH}$, rapid disk formation caused by relativistic precession is also possible for J0456−20.

4.3. X-ray and UV variability: Rapid formation and destruction of the corona and/or accretion-state transition?

As argued above, a warm and a hot corona cause the X-ray emission in the $P_{X,plat}$ phase and the bright end of the $P_{X,rise}$ phase. We find no strong evidence for such coronae at the faint end of the $P_{X,rise}$ and $P_{X,drop}$ phases, suggesting that the X-ray and UV variability could be caused by a change in the structure of the accretion flow at different accretion rates. Theoretical calculation suggests that a transition in accretion mode occurs when the accretion rate reaches critical values (Meyer et al. 2000). Strong evidence for accretion-state transitions within single AGNs remains elusive, although there are indications of multiple accretion modes in AGN samples (e.g. Gu & Cao 2009). Transitions like this have been frequently observed in BHXRBs, which typically show three states based largely on the X-ray spectral and temporal properties (Remillard & McClintock 2006). The hard state is characterised by a strong non-thermal emission in the form of a power-law photon spectrum $N(E) \propto E^{-\Gamma}$ with a photon index Γ of ∼1.4−2.1 and a weak thermal disk emission. In contrast, the X-ray emission in the soft state is dominated by thermal disk emission with weak non-thermal emission. The steep power-law (SPL) state (or the very high state) is characterised by strong non-thermal power-law component with $\Gamma > 2.4$ and also substantial thermal disk emission.

The accretion rate can change by orders of magnitude within a timescale of months to years in nuclear transients, making them the ideal objects for studying accretion-state transitions in SMBH–accreting systems. An accretion-state transition has been reported in a few TDEs. For instance, the detection of radio emission and change in X-ray spectral properties in ASASSN-14li are suggested as evidence of an accretion-state transition from hard to thermal states (van Velzen et al. 2016). Wevers et al. (2021) suggested that the observed evolution of the X-ray and UV emission of AT2018fyk can be explained by a rapid accretion-state transition between the thermal and hard states. In the following, we discuss whether the observed X-ray, UV and radio variability can be explained with accretion-state transitions in the framework of a coupling of the corona with the accretion disk.

4.3.1. Analogy to BHXRBs: Soft state when the X-ray emission is faint and SPL state when the X-ray emission is bright

As mentioned above, the X-ray spectra of J0456−20 can best be described by a multi-colour disk with T_{in} of ∼70 eV at the faint state during the X-ray rise phase. The X-ray spectrum from X1, taken soon after the rapid X-ray flux drop, is also very soft, with 99^{+120}_{-40} eV. These results suggest that the X-ray emission of J0456−20 is dominated by thermal emission from a thin disk when the X-ray flux is faint (① and ⑤ in Fig. 11 panel c), which is reminiscent of the soft state in BHXRBs. In Fig. 12 we show the location of J0456−20 during the X-ray faint state on the BHXRB hardness-intensity diagram (Fender et al. 2004).

The top panel of Fig. 8 shows that the X-ray spectra during the $P_{X,plat}$ phase and the bright end of the $P_{X,rise}$ phase can be described by a power law with a photon index in the range of ∼2.5−3.0. A thermal component, which contributes ∼26% of the total 0.2−2.0 keV band, is also detected in the high-quality X2 and X3 data. These characteristics suggest that J0456−20 is in the SPL state when the source is bright in the X-ray band (④ in Fig. 11 and 12). In addition, the X-ray
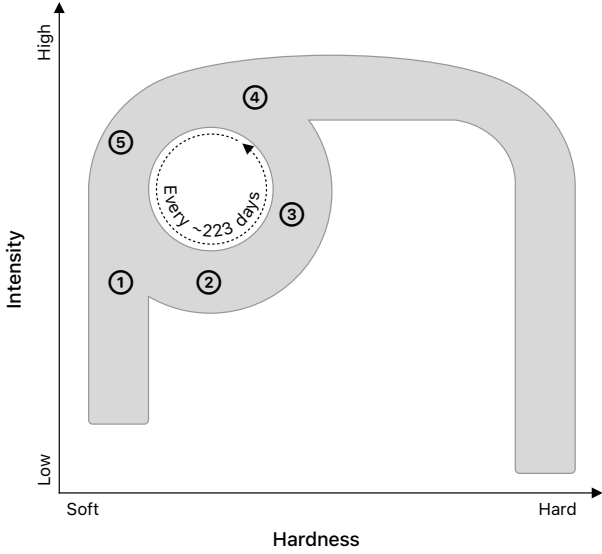
Fig. 12. States of J0456−20 overlaid on the BH X-ray binary state diagram. The numbers are as labelled in Fig. 11. The source cycles between a low soft state dominated by thermal emission (①–②), ignition of Comptonised emission (③–④), and returns to a thermally dominated state ⑤. The phase ⑥ in Fig. 11 corresponds to the quiescent state of BHXRBs and is not shown in this plot.

spectra from X2 and X3 require two Comptonisation components, a requirement that was reported in some BHXRBs in the SPL state (Gierliński & Done 2003). Perhaps the strongest support for the SPL analogy comes from the detection of radio emission in J0456−20. Unlike the compact steady jet observed in the hard state, transient radio emission from an optically thin jet is often detected at the point of accretion transition to the SPL state in BHXRBs (Fender et al. 2004). Transient radio emission like this has also been detected in J0456−20. We detected radio emission during the third plateau phase, but no radio emission was detected during the $P_{X,faint}$, $P_{X,rise}$, and $P_{X,drop}$ phases. Furthermore, the radio flux decreased by a factor of ∼3(4) within ∼2 weeks in the 9(5.5) GHz band (see Fig. 3). This is also consistent with the transient radio emission observed in the SPL state of BHXRBs, although the current radio data suggest a flat radio spectra for J0456−20, which is in contrast to the steep radio spectra observed in the SPL state in BHXRBs. Future radio observations at different flux levels are required to understand the radio emission mechanism. It also worth noting that strong high-frequency QPOs (HFQPOs) with frequencies in the range 100−450 Hz observed in BHXRBs are all detected in the SPL state (Remillard & McClintock 2006). When we assume that the frequency of HFQPOs scales inversely with M_{BH}, then the expected frequency is around $1-4.5 \times 10^{-4}$ Hz for M_{BH} of $10^7 M_\odot$, which is consistent with the tentative signal at a frequency of 2.5×10^{-4} Hz found in X2.

4.3.2. Accretion-state transition between SPL and soft states?

In the second panel of Fig. 8, we show the evolution the ratio of $f_{X,soft}$ to the 2246 Å monochromatic flux ($f_{0.2-2.0\,keV}/\nu f_{\nu(2246Å)}$), which represents the relative contribution from the corona to that of the disk (similar to the X-ray band hardness ratio used in BHXRBs) for the three cycles. It is clear from Fig. 8 that the X-ray spectrum of J0456−20 hardens (upper panel) and $f_{0.2-2.0\,keV}/\nu f_{\nu(2246Å)}$ can increase by a factor of ∼10 during the

$P_{X,rise}$ phase, suggesting that a transition from the soft state to the SPL state is taking place during the $P_{X,rise}$ phase (② and ③ in Figs. 11 and 12). This accretion-state transition is accompanied by a rapid formation of the warm and hot coronae, perhaps through the disk evaporation mechanism (Liu et al. 2002, 2003; Qiao & Liu 2015). The exact timescale of this soft-to-SPL state transition and formation of the coronae is challenging to calculate with the current data set. However, we can roughly estimate this timescale to be shorter than two months, assuming that the coronae were totally destroyed during the $P_{X,drop}$ phase and started to re-form at the beginning of the $P_{X,rise}$ phase. Accretion-state transitions have also been invoked to explain the X-ray variability in several TDEs. For instance, similar to J0456−20, the X-ray spectra of AT2018fyk (Wevers et al. 2021) and AT2021ehb (Yao et al. 2022) are very soft and likely dominated by the emission from a thermal accretion disk in the early stages. As the X-ray flux increases, the X-ray spectra of both sources gradually become harder. Interestingly, both sources also show a plateau phase in their X-ray light curves. However, the photon index of the power-law component during the X-ray plateau phase for both sources are in the range of ∼2.0−2.2, which is much harder than that in J0456−20 and is consistent with the X-ray properties of BHXRBs in the hard state (thus a soft-to-hard state transition) rather than the SPL state. No radio emission is detected in either of these two sources.

The X-ray spectrum of J0456−20 becomes softer and the $f_{0.2-2.0\,keV}/\nu f_{\nu(2246Å)}$ decreases by a factor of ≳10 during the $P_{X,drop}$ phase. We explain the $P_{X,drop}$ phase in J0456−20 by the transition from the SPL state to the soft state, which may result from the collapse or destruction of the coronae (sequence 5–6 in Fig. 11). A rapid X-ray flux drop has also been reported in a few other TDEs. For instance, a sharp flux drop (a factor of >50 in four days) has been found in the late-time X-ray light curve of the jetted TDE Swift 1644+57 (Levan et al. 2016), and is explained as the shutdown of the jet as the accretion disk transitions from a thick disk to a thin disk (e.g. Mangano et al. 2016). We do not find strong evidence for powerful jets in J0456−20, and the $P_{X,drop}$ occurred several weeks after the radio non-detection. Thus it is unlikely the $P_{X,drop}$ in J0456−20 is related to the shutdown of a jet. AT2021ehb also shows a rapid X-ray flux drop by a factor of 10 within three days, during which the X-ray spectrum becomes significantly softer. Yao et al. (2022) proposed that this rapid drop is likely due to a hard-to-soft state transition. Unlike J0456−20, the power-law component still contributed substantially to the X-ray emission of AT2021ehb after the X-ray flux drop, indicating that the corona did not change drastically. Corona destruction has been proposed to explain the X-ray flux variability in the AGN 1ES 1927+654 (Ricci et al. 2020; Masterson et al. 2022). The timescale of the SPL-to-soft transition or corona destruction in J0456−20 is shorter than a few weeks, which is similar to that found in 1ES 1927+654 (aboutone month). It is clear from Fig. 1 that the $P_{X,drop}$ phase is always followed by a sudden increase in the UV brightness, which may be attributed to a temporary increase of the accretion rate caused by the collapse of the coronae at the inner region of the disk. The physical process that triggers the SPL-to-soft transition, thus the $P_{X,drop}$ phase, is unknown. There is an indication that the $P_{X,drop}$ phase occurs at a UV faint state for cycle2 and cycle3 (see Fig. 1). However, the UV brightness showed very different evolution before the $P_{X,drop}$ between cycle2 (decline on a timescale of weeks) and cycle3 (almost constant, but also showed variability within a week). Thus it is currently unclear whether the $P_{X,drop}$ and the UV faint state are connected.

By studying the X-ray and UV properties of a sample of seven X-ray bright TDEs, Wevers (2020) found that the X-ray emission of TDEs with $\lambda_{\rm Edd} \gtrsim 0.03$ is dominated by the thermal emission, whereas the power-law component dominates the X-ray emission for TDEs with $\lambda_{\rm Edd} \lesssim 0.03$. They also found that, similar to BHXRBs and AGNs, the X-ray spectral state transition occurs around $\lambda_{\rm Edd} \approx 0.03$. For J0456−20, the X-ray spectrum from Swift5, during which J0456−20 has a $\lambda_{\rm Edd}$ of 0.07, is indeed dominated by thermal emission. However, as $\lambda_{\rm Edd}$ increases from 0.07 (Swift5) to a peak value of ∼0.23 in cycle2, the contribution from the power-law component increases, and the power-law component dominates the X-ray emission (see the second panel of Fig. 8 and also Fig. 10). Although contrary to the general trend found in Wevers (2020), our results are consistent with that found in AT2021ehb during its X-ray rising phase (Yao et al. 2022), suggesting that the dependence of X-ray spectral state on $\lambda_{\rm Edd}$ may vary from source to source. In addition, accretion-state transitions between the soft and hard states in BHXRBs can happen in a wide range of $\lambda_{\rm Edd}$. For instance, Tetarenko et al. (2016) found that the hard-to-soft transition of a sample of BHXRBs occurs at around $\log(\lambda_{\rm Edd}) = -0.94$ with a standard deviation of 0.41. The hard-to-soft transition can happen in a wide range of $\lambda_{\rm Edd}$ even for individual BHXRBs (e.g. H1743−322, Coriat et al. 2011). The soft-to-hard state transition normally happens at a lower $\lambda_{\rm Edd}$ with $\log(\lambda_{\rm Edd}) = -1.5$ (standard deviation of 0.37, Tetarenko et al. 2016). The peak $\lambda_{\rm Edd}$ of J0456−20 monotonically decreases from ∼0.37 in cycle1 to ∼0.07 in cycle3, which indicates that the accretion-state transitions between soft and SPL states may also occur at very different $\lambda_{\rm Edd}$ in accreting SMBH systems. Finally, the similarity between J0456−20 and the X-ray light curves of some BHXRBs is worth noting (e.g. GRO J1655−40, Sobczak et al. 1999, and 4U 1630−47, Abe et al. 2005). In particular, the evolution of the X-ray light curve of J0456−20 shows remarkable similarity to GRO J1655−40 (e.g. Fig. 1 in Sobczak et al. 1999 and Fig. 4a in Remillard & McClintock 2006), which was in an outburst in 1996–1997. After the outburst, GRO J1655−40 initially brightened in the soft state for 50 days until it entered a plateau-like phase. The source then stayed in this phase for about five months, during which the spectrum was reminiscent of the SPL state (SPL, or very high state). It then quickly went into a faint state within two weeks. The resemblance provides further evidence that similar accretion processes are at work for SMBH and stellar mass BH accreting systems.

5. Summary

We presented the detailed multi-wavelength analysis of the pTDE candidate eRASSt J045650.3−203750, which is located in the nucleus of a quiescent galaxy at $z = 0.077$. The main observed features are listed below.

1. J0456−20 likely is a repeating nuclear transient that shows four distinctive X-ray phases. We observed three cycles so far. The tentatively estimated recurrence time is ∼223 days.
2. The most prominent feature of J0456−20 is the drastic X-ray flux decline by a factor of $\gtrsim 100$ within one week during the X-ray flux drop phase. Before this rapid X-ray flux drop phase, the X-ray flux of J0456−20 is in the X-ray plateau phase, which can last for abouttwo months. After the rapid X-ray flux drop phase, J0456−20 goes into the X-ray faint state for about twotothree months before the X-ray rising phase starts again.
3. The X-ray spectra are generally very soft in the X-ray rising phase, with a photon index $\gtrsim 3.0$ and evidence of a multi-colour disk with a temperature of ∼70 eV at the faint end of this phase. The X-ray spectra become slightly harder during the X-ray plateau phase, with a photon index $\lesssim 3.0$.
4. Non-thermal components are clearly seen in the high-quality *XMM-Newton* data during the plateau phase and also at the bright end of the rising phase. These non-thermal components are likely produced via inverse Comptonisation of soft seed photons by a warm and hot corona.
5. J0456−20 showed only moderate UV variability and no significant optical variability. The optical spectra taken at different X-ray phases are always consistent with a typical quiescent galaxy with no indication of emission lines.
6. Radio emission, which decreases rapidly on a timescale of two weeks, has been detected only in the X-ray plateau phase (as of now).

J0456−20 is an exceptional repeating nuclear transient discovered with eROSITA. We discussed several scenarios to explain the cause of the repeating X-ray flares in J0456−20: a repeating partial TDE, a pair of EMRIs, and radiation pressure instability. We favour a repeating pTDE as the most plausible scenario. The mass loss is estimated to be 0.05 $M_\odot$, 0.015 $M_\odot$, and 0.005 $M_\odot$ for the first, second, and third cycle, respectively. These values are low enough for a pTDE. The observed peak rest-frame 0.2−2.0 keV luminosity decreases monotonically from the first cycle (∼1.6×10^{44} erg s^{-1}) to the third cycle (∼3.0×10^{43} erg s^{-1}). This also agrees with the expectation from a pTDE. Long-term multi-wavelength monitoring in the future is required to further support the pTDE scenario and to accurately measure the recurrence time. Our analysis shows that the X-ray/UV emission is dominated by thermal emission from a thin accretion disk when the X-ray flux is faint, which is reminiscent of the soft state in BHXRBs. The thermal disk still causes the UV emission in the X-ray bright state. The X-ray emission, however, is dominated by X-ray photons from the inverse Comptonisation of the soft photons by a warm and a hot corona. In addition, the X-ray spectral property and the detection of transient radio emission suggest that J0456−20 is in the SPL state when the source is bright in the X-ray band. We propose that a transition from the soft state to the SPL state, accompanied by the formation of the warm and hot coronae, can explain the X-ray rising phase, while the rapid X-ray flux drop is caused by a transition from the SPL state to the soft state, during which the coronae are destroyed. High-cadence X-ray and UV observations, particularly during the rapid X-ray flux drop phase, are needed to further understand the evolution of the thermal and non-thermal emission in J0456−20. This may provide new clues for the accretion-state transition in SMBH–accreting systems and for the formation and destruction of the corona. J0456−20 shows transient radio emission with rapid variability on a timescale of a few weeks, which is rare in nuclear transients. Future radio observations at multiple frequencies are crucial for understanding the mechanism for the radio emission in J0456−20.

References

Abe, Y., Fukazawa, Y., Kubota, A., Kasama, D., & Makishima, K. 2005, PASJ, 57, 629

Alexander, D. M., & Hickox, R. C. 2012, New A Rv., 56, 93

Alexander, K. D., Berger, E., Guillochon, J., Zauderer, B. A., & Williams, P. K. G. 2016, ApJ, 819, L25

Alexander, K. D., van Velzen, S., Horesh, A., & Zauderer, B. A. 2020, Space Sci. Rev., 216, 81

Amaro-Seoane, P., Miller, M. C., & Kennedy, G. F. 2012, MNRAS, 425, 2401

Appenzeller, I., Fricke, K., Fürtig, W., et al. 1998, The Messenger, 94, 1

Arcodia, R., Merloni, A., Nandra, K., et al. 2021, Nature, 592, 704

Arnaud, K. A. 1996, ASP Conf. Ser., 101, 17

Bellm, E. C., Kulkarni, S. R., Graham, M. J., et al. 2019, PASP, 131, 018002

Belloni, T., & Hasinger, G. 1990, A&A, 230, 103

Belloni, T., Méndez, M., King, A. R., van der Klis, M., & van Paradijs, J. 1997, ApJ, 479, L145

Bertin, E. 2006, in Astronomical Data Analysis Software and Systems XV, eds. C. Gabriel, C. Arviset, D. Ponz, & S. Enrique, ASP Conf. Ser., 351, 112

Bloom, J. S., Giannios, D., Metzger, B. D., et al. 2011, Science, 333, 203

Brunner, H., Liu, T., Lamer, G., et al. 2022, A&A, 661, A1

Buckley, D. A. H., Swart, G. P., & Meiring, J. G. 2006, in Ground-based and Airborne Telescopes, ed. L. M. Stepp, SPIE Conf. Ser., 6267, 62670Z

Burgh, E. B., Nordsieck, K. H., Kobulnicky, H. A., et al. 2003, in Instrument Design and Performance for Optical/Infrared Ground-based Telescopes, eds. M. Iye, A. F. M. Moorwood, SPIE Conf. Ser., 4841, 1463

Buzzoni, B., Delabre, B., Dekker, H., et al. 1984, The Messenger, 38, 9

Campana, S., Mainetti, D., Colpi, M., et al. 2015, A&A, 581, A17

Cappellari, M. 2017, MNRAS, 466, 798

Cash, W. 1979, ApJ, 228, 939

Cendes, Y., Alexander, K. D., Berger, E., et al. 2021, ApJ, 919, 127

Cendes, Y., Berger, E., Alexander, K. D., et al. 2022, ApJ, 938, 28

Chambers, K. C., Magnier, E. A., Metcalfe, N., et al. 2016, ArXiv e-prints [arXiv:1612.05560]

Childress, M. J., Vogt, F. P. A., Nielsen, J., & Sharp, R. G. 2014, Ap&SS, 349, 617

Coriat, M., Corbel, S., Prat, L., et al. 2011, MNRAS, 414, 677

Coughlin, E. R., & Nixon, C. J. 2019, ApJ, 883, L17

Crawford, S. M., Still, M., Schellart, P., et al. 2010, in Observatory Operations: Strategies, Processes, and Systems III, eds. D. R. Silva, A. B. Peck, & B. T. Soifer, SPIE Conf. Ser., 7737, 773725

Cufari, M., Coughlin, E. R., & Nixon, C. J. 2022, ApJ, 929, L20

Dai, L., McKinney, J. C., Roth, N., Ramirez-Ruiz, E., & Miller, M. C. 2018, ApJS, 859, L20

Dopita, M., Rhee, J., Farage, C., et al. 2010, Ap&SS, 327, 245

Evans, C. R., & Kochanek, C. S. 1989, ApJ, 346, L13

Evans, P. A., Beardmore, A. P., Page, K. L., et al. 2009, MNRAS, 397, 1177

Evans, P. A., Page, K. L., Osborne, J. P., et al. 2020, ApJS, 247, 54

Fender, R. P., Belloni, T. M., & Gallo, E. 2004, MNRAS, 355, 1105

Ferrarese, L., & Merritt, D. 2000, ApJ, 539, L9

Freudling, W., Romaniello, M., Bramich, D. M., et al. 2013, A&A, 559, A96

Gabriel, C., Denby, M., Fyfe, D. J., et al. 2004, in Astronomical Data Analysis Software and Systems (ADASS) XIII, eds. F. Ochsenbein, M. G. Allen, & D. Egret, ASP Conf. Ser., 314, 759

Gebhardt, K., Bender, R., Bower, G., et al. 2000, ApJ, 539, L13

Gendreau, K. C., Arzoumanian, Z., Adkins, P. W., et al. 2016, in Space Telescopes and Instrumentation 2016: Ultraviolet to Gamma Ray, eds. J. W. A. den Herder, T. Takahashi, & M. Bautz, SPIE Conf. Ser., 9905, 99051H

Gierliński, M., & Done, C. 2003, MNRAS, 342, 1083

Giustini, M., Miniutti, G., & Saxton, R. D. 2020, A&A, 636, L2

Goodwin, A. J., van Velzen, S., Miller-Jones, J. C. A., et al. 2022, MNRAS, 511, 5328

Grupe, D., Komossa, S., & Saxton, R. 2015, ApJ, 803, L28

Gu, M., & Cao, X. 2009, MNRAS, 399, 349

Guillochon, J., & Ramirez-Ruiz, E. 2013, ApJ, 767, 25

Gültekin, K., Richstone, D. O., Gebhardt, K., et al. 2009, ApJ, 698, 198

Hayasaki, K., Stone, N., & Loeb, A. 2013, MNRAS, 434, 909

Hills, J. G. 1988, Nature, 331, 687

Jin, C. 2021, ApJ, 920, 60

Jin, C., Done, C., & Ward, M. 2021, MNRAS, 500, 2475

Kaastra, J. S., & Bleeker, J. A. M. 2016, A&A, 587, A151

Kankare, E., Kotak, R., Mattila, S., et al. 2017, Nat. Astron., 1, 865

Komossa, S. 2015, J. High Energy Astrophys., 7, 148

Komossa, S., & Bade, N. 1999, A&A, 343, 775

Kool, E. C., Reynolds, T. M., Mattila, S., et al. 2020, MNRAS, 498, 2167

Kormendy, J., & Ho, L. C. 2013, ARA&A, 51, 511

Kormendy, J., & Richstone, D. 1995, ARA&A, 33, 581

Kraft, R. P., Burrows, D. N., & Nousek, J. A. 1991, ApJ, 374, 344

Law, N. M., Kulkarni, S. R., Dekany, R. G., et al. 2009, PASP, 121, 1395

Levan, A. J., Tanvir, N. R., Cenko, S. B., et al. 2011, Science, 333, 199

Levan, A. J., Tanvir, N. R., Brown, G. C., et al. 2016, ApJ, 819, 51

Liu, B. F., Mineshige, S., & Shibata, K. 2002, ApJ, 572, L173

Liu, B. F., Mineshige, S., & Ohsuga, K. 2003, ApJ, 587, 571

Liu, Z., Liu, H.-Y., Cheng, H., Qiao, E., & Yuan, W. 2020, MNRAS, 492, 2335

Lu, W., & Bonnerot, C. 2020, MNRAS, 492, 686

Magorrian, J., Tremaine, S., Richstone, D., et al. 1998, AJ, 115, 2285

Malyali, A., Rau, A., Merloni, A., et al. 2021, A&A, 647, A9

Mangano, V., Burrows, D. N., Sbarufatti, B., & Cannizzo, J. K. 2016, ApJ, 817, 103

Masterson, M., Kara, E., Ricci, C., et al. 2022, ApJ, 934, 35

Mattila, S., Pérez-Torres, M., Efstathiou, A., et al. 2018, Science, 361, 482

McMullin, J. P., Waters, B., Schiebel, D., Young, W., & Golap, K. 2007, in Astronomical Data Analysis Software and Systems XVI, eds. R. A. Shaw, F. Hill, & D. J. Bell, ASP Conf. Ser., 376, 127

Merloni, A., & Heinz, S. 2013, in Planets, Stars and Stellar Systems, Volume 6: Extragalactic Astronomy and Cosmology, eds. T. D. Oswalt, & W. C. Keel, 6, 503

Metzger, B. D., & Stone, N. C. 2017, ApJ, 844, 75

Metzger, B. D., Stone, N. C., & Gilbaum, S. 2022, ApJ, 926, 101

Meyer, F., Liu, B. F., & Meyer-Hofmeister, E. 2000, A&A, 354, L67

Miniutti, G., Saxton, R. D., Giustini, M., et al. 2019, Nature, 573, 381

Nandra, K., George, I. M., Mushotzky, R. F., Turner, T. J., & Yaqoob, T. 1997, ApJ, 476, 70

Narayan, R., & Yi, I. 1995, ApJ, 452, 710

Noda, H., & Done, C. 2018, MNRAS, 480, 3898

Pan, H.-W., Yuan, W., Zhou, X.-L., Dong, X.-B., & Liu, B. 2015, ApJ, 808, 163

Pan, X., Li, S.-L., & Cao, X. 2021, ApJ, 910, 97

Payne, A. V., Shappee, B. J., Hinkle, J. T., et al. 2021, ApJ, 910, 125

Piran, T., Svirski, G., Krolik, J., Cheng, R. M., & Shiokawa, H. 2015, ApJ, 806, 164

Planck Collaboration VI. 2020, A&A, 641, A6

Ponti, G., Papadakis, I., Bianchi, S., et al. 2012, A&A, 542, A83

Predehl, P., Andritschke, R., Arefiev, V., et al. 2021, A&A, 647, A1

Prochaska, J. X., Hennawi, J. F., Westfall, K. B., et al. 2020, J. Open Source Softw., 5, 2308

Qiao, E., & Liu, B. F. 2015, MNRAS, 448, 1099

Rees, M. 1988, J., 333, 523

Remillard, R. A., & McClintock, J. E. 2006, ARA&A, 44, 49

Remillard, R. A., Loewenstein, M., Steiner, J. F., et al. 2022, AJ, 163, 130
Ricci, C., Kara, E., Loewenstein, M., et al. 2020, ApJ, 898, L1
Ruiz, A., Georgakakis, A., Gerakakis, S., et al. 2022, MNRAS, 511, 4265
Ryu, T., Krolik, J., Piran, T., & Noble, S. C. 2020a, ApJ, 904, 98
Ryu, T., Krolik, J., Piran, T., & Noble, S. C. 2020b, ApJ, 904, 99
Ryu, T., Krolik, J., Piran, T., & Noble, S. C. 2020c, ApJ, 904, 100
Saxton, R. D., Motta, S. E., Komossa, S., & Read, A. M. 2015, MNRAS, 454, 2798
Saxton, R., Komossa, S., Auchettl, K., & Jonker, P. G. 2021, Space Sci. Rev., 217, 18
Sazonov, S., Gilfanov, M., Medvedev, P., et al. 2021, MNRAS, 508, 3820
Schlafly, E. F., & Finkbeiner, D. P. 2011, ApJ, 737, 103
Shakura, N. I., & Sunyaev, R. A. 1973, A&A, 24, 337
Sniegowska, M., Czerny, B., Bon, E., & Bon, N. 2020, A&A, 641, A167
Sobczak, G. J., McClintock, J. E., Remillard, R. A., Bailyn, C. D., & Orosz, J. A. 1999, ApJ, 520, 776
Strüder, L., Briel, U., Dennerl, K., et al. 2001, A&A, 365, L18
Sunyaev, R., Arefiev, V., Babyshkin, V., et al. 2021, A&A, 656, A132
Tetarenko, B. E., Sivakoff, G. R., Heinke, C. O., & Gladstone, J. C. 2016, ApJS, 222, 15
Timmer, J., & Koenig, M. 1995, A&A, 300, 707
Tonry, J. L., Denneau, L., Heinze, A. N., et al. 2018, PASP, 130, 064505

Trakhtenbrot, B., Arcavi, I., Ricci, C., et al. 2019, Nat. Astron., 3, 242
Turner, M. J. L., Abbey, A., Arnaud, M., et al. 2001, A&A, 365, L27
Valdes, F., Gupta, R., Rose, J. A., Singh, H. P., & Bell, D. J. 2004, ApJS, 152, 251
van Velzen, S., Anderson, G. E., Stone, N. C., et al. 2016, Science, 351, 62
van Velzen, S., Holoien, T. W. S., Onori, F., Hung, T., & Arcavi, I. 2020, Space Sci. Rev., 216, 124
Vaughan, S. 2010, MNRAS, 402, 307
Vaughan, S., Uttley, P., Markowitz, A. G., et al. 2016, MNRAS, 461, 3145
Wevers, T. 2020, MNRAS, 497, L1
Wevers, T., Pasham, D. R., van Velzen, S., et al. 2019, MNRAS, 488, 4816
Wevers, T., Pasham, D. R., van Velzen, S., et al. 2021, ApJ, 912, 151
Willingale, R., Starling, R. L. C., Beardmore, A. P., Tanvir, N. R., & O'Brien, P. T. 2013, MNRAS, 431, 394
Wilms, J., Allen, A., & McCray, R. 2000, ApJ, 542, 914
Yao, Y., Lu, W., Guolo, M., et al. 2022, ApJ, 937, 8
Yuan, F., & Narayan, R. 2014, ARA&A, 52, 529
Yuan, W., Komossa, S., Xu, D., et al. 2004, MNRAS, 353, L29
Zabludoff, A., Arcavi, I., La Massa, S., et al. 2021, Space Sci. Rev., 217, 54
Zauderer, B. A., Berger, E., Soderberg, A. M., et al. 2011, Nature, 476, 425
Zauderer, B. A., Berger, E., Margutti, R., et al. 2013, ApJ, 767, 152

Appendix A: False-colour image of the host galaxy and astrometric correction

Fig. A.1 shows the false-colour image of the host galaxy. The image is composited based on the Canada–France–Hawaii Telescope (CFHT) MegaCam *gri* images. For the CFHT images, astrometric correction was performed using the SCAMP software (Bertin et al. 2006). The PanSTARRS1-DR1 catalogue was used as the reference catalogue. The *XMM-Newton* coordinates were estimated from the EPIC/pn data of X2. The Swift5 UVOT observation, which has a long exposure time, was used to determine the location of the UV flare. The UVOT image was also corrected for astrometry using the PanSTARRS1-DR1 catalogue as reference. The position of the UV flare is (RA, Dec) = (04h56m49.81s, −20°37′47.99″), with a 1σ uncertainty of 0.4″. The UV position is consistent with the X-ray positions measured from eRASS3 and X2.
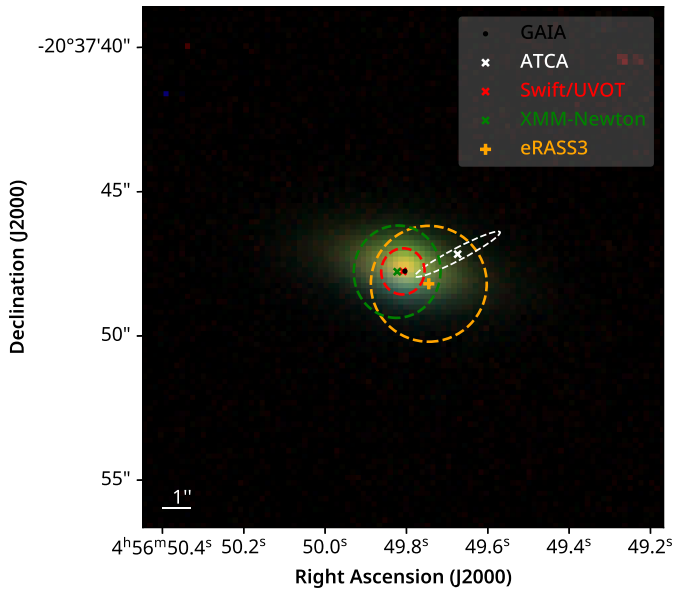
Fig. A.1. False-colour image of the host galaxy, composited from the CFHT MegaCam *gri* images. The black dot marks the position given in GAIA EDR3. The crosses represent the positions measured from different instruments, and the circles indicate the 2σ positional uncertainties: *Swift*/UVOT (red, $2\sigma = 0.8″$), ATCA (white, see Sect. 2.6), *XMM-Newton* (green, $2\sigma = 1.6″$), and eRASS3 (orange, $2\sigma = 2.0″$).

Appendix B: Estimating the upper limit of the X-ray flux

To calculate the upper limit of J0456−20 flux in eRASS1, we first adopted the Bayesian approach presented in Kraft et al. (1991) to estimate the photon count upper limit at a given confidence level. Following the suggestion in Ruiz et al. (2022), we chose a single-side confidence level of 0.9987 (this corresponds to a double-side confidence level of 0.997) to estimate the 3σ upper limit. Using the source and background regions defined for eRASS2, we measured total and background photon counts of 2 and 0.54, respectively, in the $0.2 − 2.3$ keV energy band. Based on the exposure time of 325 s for eRASS1, this resulted in a 3σ count-rate upper limit of 0.04 s^{-1} after correcting for the encircled energy fraction (EEF), which measures the fraction of total source photons within the source region (EEF ~ 0.8 for J0456−20 in eRASS1). We then calculated the unabsorbed intrinsic flux upper limit over the $0.2 − 2.0$ keV energy band for eRASS1. We converted the source photon count rate into flux using the M_{ul} model. We derived a 3σ upper limit of 2.2×10^{-13} erg cm^{-2} s^{-1}. We did not include the host galaxy absorption as no evidence for significant host galaxy absorption was found in the high-quality *XMM-Newton* data (see Sect. 3.3.1).

Appendix C: Observation log and details of the UV and X-ray observation

Table C.1. *Swift*/UVOT and *XMM-Newton*/OM observation log of J0456−20. MJD is the mid-date of the coverage for each observation; $T_{\rm exp}$ is the effective exposure time in units of seconds; $m_{\rm AB}$ is the apparent AB magnitude with the UVM2 filter; f_λ is the UVM2 flux density in units of $10^{-17}\,{\rm erg\,cm^{-2}\,s^{-1}\,\AA^{-1}}$. Quoted uncertainties are at the 1σ confidence level; $N_{\rm sigma}$ is the detection significance. For observations with $N_{\rm sigma} < 3.0$, the values of the 3σ upper limits are given for $m_{\rm AB}$ and f_λ; ObsID is the observation ID for each observation.

MJD	$T_{\rm exp}$	$m_{\rm AB}$	f_λ	$N_{\rm sigma}$	ObsID	Instrument
59284.89	1659	22.16 ± 0.28	3.0 ± 0.8	3.8	00014135001	*Swift*
59300.20	11800	21.07 ± 0.18	7.56 ± 1.01	9.7	0862770201	*XMM-Newton*
59320.20	3201	21.01 ± 0.09	8.7 ± 0.7	12.3	00014135002	*Swift*
59329.73	3285	21.10 ± 0.10	8.0 ± 0.7	11.9	00014135003	*Swift*
59340.45	1375	21.63 ± 0.20	5.0 ± 0.9	5.5	00014135004	*Swift*
59391.16	7628	21.64 ± 0.09	4.9 ± 0.4	12.1	00014135005	*Swift*
59399.00	6347	21.50 ± 0.09	5.5 ± 0.4	12.5	00014135006	*Swift*
59405.13	1778	21.41 ± 0.16	6.0 ± 0.9	7.1	00014135007	*Swift*
59413.03	1623	21.43 ± 0.17	5.9 ± 0.9	6.4	00014135008	*Swift*
59427.10	1609	21.64 ± 0.19	4.9 ± 0.8	5.8	00014135009	*Swift*
59434.71	1936	21.73 ± 0.19	4.5 ± 0.8	5.7	00014135010	*Swift*
59447.51	51100	21.99 ± 0.16	3.01 ± 0.47	8.7	0891801101	*XMM-Newton*
59453.89	2914	21.82 ± 0.17	4.1 ± 0.6	6.5	00014135011	*Swift*
59468.45	438	< 21.59	< 5.1	2.5	00014135012	*Swift*
59472.51	2504	21.85 ± 0.18	4.0 ± 0.7	6.0	00014135013	*Swift*
59481.30	127500	22.91 ± 0.19	1.27 ± 0.24	7.4	0891801701	*XMM-Newton*
59481.49	2458	22.33 ± 0.25	2.6 ± 0.6	4.5	00014135014	*Swift*
59496.67	3034	22.66 ± 0.29	1.9 ± 0.5	3.7	00014135016	*Swift*
59510.83	2738	22.49 ± 0.26	2.2 ± 0.5	4.1	00014135017	*Swift*
59524.53	1349	21.74 ± 0.21	4.5 ± 0.8	5.3	00014135018	*Swift*
59527.63	1401	21.88 ± 0.24	3.9 ± 0.8	4.6	00014135019	*Swift*
59529.87	440	21.63 ± 0.33	4.9 ± 1.5	3.3	00014135021	*Swift*
59543.72	1045	21.32 ± 0.17	6.6 ± 1.0	6.3	00014135022	*Swift*
59557.41	2288	21.64 ± 0.15	4.9 ± 0.7	7.2	00014135023	*Swift*
59566.74	604	21.36 ± 0.26	6.3 ± 1.5	4.3	00014135025	*Swift*
59572.58	2591	21.46 ± 0.13	5.7 ± 0.7	8.7	00014135026	*Swift*
59584.90	2835	21.74 ± 0.15	4.5 ± 0.6	7.5	00014135027	*Swift*
59635.12	9989	21.91 ± 0.10	3.8 ± 0.3	11.7	00014135999[a]	*Swift*
59643.68	2452	21.96 ± 0.20	3.6 ± 0.7	5.4	00014135033	*Swift*
59650.19	2935	22.61 ± 0.29	2.0 ± 0.5	3.8	00014135034	*Swift*
59656.16	2640	22.11 ± 0.21	3.1 ± 0.6	5.3	00014135036	*Swift*
59663.24	2734	22.28 ± 0.25	2.7 ± 0.6	4.5	00014135037	*Swift*
59670.56	3088	22.01 ± 0.20	3.5 ± 0.6	5.5	00014135038	*Swift*
59678.08	4241	22.25 ± 0.20	2.7 ± 0.5	5.6	00014135039	*Swift*
59684.37	2894	22.16 ± 0.22	3.0 ± 0.6	4.9	00014135040	*Swift*
59691.98	6307	22.05 ± 0.14	3.4 ± 0.4	7.8	00014135041	*Swift*
59698.54	2592	< 22.63	< 2.0	2.2	00014135042	*Swift*
59705.34	2443	22.22 ± 0.26	2.9 ± 0.7	4.2	00014135043	*Swift*

Notes. [a]This is a surrogate ObsID that consists of three observations with ObsIDs of 00014135030, 00014135031, and 00014135032.

Table C.2. Log of X-ray observations of J0456−20. MJD is the mid-date of the coverage for each observation; T_{exp} is the effective exposure time in units of seconds. Exposure for *XMM-Newton* ObsID 0862770201 is calculated from combined MOS data, while the pn exposures are given for the other *XMM-Newton* observations; CR_{total} and CR_{bkg} are respectively the total and background photon counts rate calculated over the $0.3 − 5.0$ keV band for *Swift*, $0.2 − 2.3$ keV band for eROSITA, $0.3 − 1.0$ keV band for NICER detections and $0.4 − 1.0$ keV for non-detections (avoid potential contribution from optical loading), and $0.2 − 6.0$ keV for *XMM-Newton*. For *XMM-Newton* ObsID 0862770201, count rates from the combined MOS data are given, while the count rates from the pn data are given for the other *XMM-Newton* observations; T_{in}/Γ: The inner temperature of a multi-color disk is given for eRASS2, *Swift* observation 00014135005 (Swift5), and *XMM-Newton* observation 0862770201. The photon index of the power-law is given for the other observations. A value without an uncertainty means that the parameter is fixed at the given value during spectral fitting; $f_{X,soft}$ is the rest frame intrinsic $0.2 − 2.0$ keV flux in units of 10^{-12} erg cm^{-2} s^{-1}. The 3σ upper limits are given for observations in which the J0456−20 is not detected; ObsID is the observation ID for each observation. Quoted uncertainties are at the 90% confidence level.

MJD	T_{exp} (s)	CR_{total} (cts s^{-1})	CR_{bkg} (cts s^{-1})	T_{in}/Γ (eV/-)	$f_{X,soft}$ 10^{-12} erg cm^{-2} s^{-1}	ObsID	Instrument
58919.15	325	0.00616	0.00167	3.0	< 0.22	eRASS1	eROSITA
59101.73	340	0.03534	0.00107	$64._{-18.}^{+29.}$	$0.51_{-0.26}^{+0.51}$	eRASS2	eROSITA
59272.63	194	2.22111	0.01939	$2.5_{-0.2}^{+0.2}$	$7.76_{-0.76}^{+0.84}$	eRASS3-1	eROSITA
59281.86	123	2.35918	0.02659	$2.8_{-0.2}^{+0.2}$	$11.3_{-1.40}^{+1.61}$	eRASS3-2	eROSITA
59284.89	1683	0.21745	0.00110	$2.5_{-0.1}^{+0.1}$	$11.6_{-1.45}^{+1.66}$	00014135001	*Swift*
59290.94	1664	0.21575	0.20971	3.0	< 0.19	4604010101	NICER
59291.53	9941	0.17916	0.17999	3.0	< 0.13	4604010102	NICER
59292.21	6394	0.19706	0.19072	3.0	< 0.14	4604010103	NICER
59298.15	4387	0.29770	0.25157	3.0	< 0.18	4604010201	NICER
59300.20	10040	0.00159	0.00047	99_{-40}^{+120}	$0.03_{-0.02}^{+0.06}$	0862770201	*XMM-Newton*
59305.09	2735	0.22157	0.25379	3.0	< 0.20	4604010301	NICER
59320.20	3254	0.00000	0.00009	3.0	< 0.28	00014135002	*Swift*
59322.59	1808	0.31029	0.36862	3.0	< 0.30	4604010501	NICER
59323.49	4525	0.24840	0.28309	3.0	< 0.21	4604010502	NICER
59325.27	230	0.14348	0.14935	3.0	< 0.35	4604010504	NICER
59328.31	420	0.15476	0.12096	3.0	< 0.24	4604010507	NICER
59329.73	3342	0.00000	0.00007	3.0	< 0.24	00014135003	*Swift*
59340.45	1402	0.00000	0.00007	3.0	< 0.54	00014135004	*Swift*
59391.16	7669	0.00065	0.00004	78	$0.18_{-0.11}^{+0.18}$	00014135005	*Swift*
59399.00	6406	0.00250	0.00015	$4.3_{-1.1}^{+1.3}$	$0.47_{-0.27}^{+0.70}$	00014135006	*Swift*
59405.13	1793	0.00558	0.00014	$5.1_{-1.6}^{+1.9}$	$1.65_{-1.14}^{+4.34}$	00014135007	*Swift*
59413.03	1641	0.01402	0.00037	$2.6_{-0.7}^{+0.7}$	$0.68_{-0.29}^{+0.53}$	00014135008	*Swift*
59422.51	3282	0.99116	0.32306	$3.7_{-0.3}^{+0.3}$	$2.77_{-0.42}^{+0.58}$	4595020102	NICER
59423.35	1597	0.99249	0.22507	$3.7_{-0.3}^{+0.3}$	$3.47_{-0.60}^{+0.86}$	4595020103	NICER
59426.30	2093	1.21739	0.32895	$3.9_{-0.3}^{+0.3}$	$3.97_{-0.66}^{+0.93}$	4595020104	NICER
59427.10	1631	0.02024	0.00022	$2.9_{-0.5}^{+0.6}$	$1.21_{-0.45}^{+0.74}$	00014135009	*Swift*
59428.95	2879	1.22612	0.38511	$3.3_{-0.3}^{+0.3}$	$3.17_{-0.43}^{+0.60}$	4595020105	NICER
59431.03	2131	1.15767	0.21195	$4.0_{-0.3}^{+0.3}$	$4.82_{-0.83}^{+1.17}$	4595020106	NICER
59432.96	764	1.01047	0.17102	$4.0_{-0.4}^{+0.4}$	$4.20_{-0.91}^{+1.40}$	4595020107	NICER
59433.12	999	1.04304	0.19543	$3.7_{-0.4}^{+0.4}$	$3.73_{-0.72}^{+1.08}$	4595020108	NICER
59434.71	1968	0.03100	0.00022	$3.5_{-0.5}^{+0.5}$	$3.07_{-0.96}^{+1.45}$	00014135010	*Swift*
59441.95	104	1.82692	0.35394	$3.8_{-0.7}^{+0.7}$	$5.96_{-1.63}^{+2.81}$	4595020109	NICER
59445.50	1760	2.15909	0.24284	$3.3_{-0.3}^{+0.3}$	$6.83_{-0.96}^{+1.36}$	4595020111	NICER
59447.51	40200	1.46844	0.01909	—	$4.79_{-0.90}^{+1.10}$	0891801101	*XMM-Newton*
59448.38	1169	1.92729	0.17791	$3.0_{-0.3}^{+0.3}$	$5.10_{-0.56}^{+0.76}$	4595020112	NICER
59453.89	2954	0.05822	0.00064	$2.8_{-0.2}^{+0.2}$	$3.20_{-0.59}^{+0.72}$	00014135011	*Swift*
59460.31	345	0.93832	0.01655	$3.4_{-0.2}^{+0.2}$	$5.26_{-0.67}^{+0.76}$	eRASS4	eROSITA
59467.45	1568	0.99490	0.20285	$2.8_{-0.3}^{+0.3}$	$2.39_{-0.29}^{+0.42}$	4604010901	NICER
59468.45	445	0.02924	0.00037	$2.9_{-0.9}^{+0.9}$	$1.73_{-0.91}^{+2.05}$	00014135012	*Swift*
59470.50	341	1.07625	0.70582	$4.1_{-0.9}^{+1.1}$	$1.67_{-0.61}^{+1.21}$	4604010902	NICER
59472.51	2542	0.03029	0.00038	$2.6_{-0.4}^{+0.4}$	$1.71_{-0.44}^{+0.61}$	00014135013	*Swift*
59476.22	1560	0.69231	0.26452	$2.9_{-0.4}^{+0.4}$	$1.23_{-0.17}^{+0.24}$	4604010903	NICER

Table C.2. continued.

MJD	$T_{\rm exp}$ (s)	$CR_{\rm total}$ (cts s^{-1})	$CR_{\rm bkg}$ (cts s^{-1})	$T_{\rm in}/\Gamma$ (eV/-)	$f_{\rm X,soft}$ 10^{-12} erg cm^{-2} s^{-1}	ObsID	Instrument
59479.33	929	1.16039	0.18996	$3.0^{+0.3}_{-0.3}$	$2.81^{+0.49}_{-0.35}$	4604010904	NICER
59481.30	85960	0.78391	0.01568	—	$2.40^{+0.76}_{-0.36}$	0891801701	*XMM-Newton*
59481.49	2490	0.02611	0.00026	$2.7^{+0.4}_{-0.4}$	$1.48^{+0.58}_{-0.41}$	00014135014	*Swift*
59482.46	4637	0.88851	0.15370	$2.9^{+0.3}_{-0.26}$	$2.33^{+0.37}_{-0.26}$	4604010905	NICER
59485.04	1183	0.96196	0.22790	$2.7^{+0.3}_{-0.3}$	$2.03^{+0.31}_{-0.23}$	4604010906	NICER
59488.08	1532	1.19648	0.32618	$3.0^{+0.3}_{-0.3}$	$2.78^{+0.57}_{-0.38}$	4604010907	NICER
59491.05	1410	1.34965	0.35106	$2.7^{+0.3}_{-0.3}$	$2.94^{+0.49}_{-0.34}$	4604010908	NICER
59494.25	811	1.13933	0.21393	$2.5^{+0.3}_{-0.3}$	$2.34^{+0.31}_{-0.24}$	4604010909	NICER
59496.67	3079	0.03085	0.00032	$2.7^{+0.3}_{-0.3}$	$2.05^{+0.64}_{-0.49}$	00014135016	*Swift*
59497.25	1133	1.13945	0.20779	$2.9^{+0.3}_{-0.3}$	$2.63^{+0.44}_{-0.31}$	4604010910	NICER
59499.80	1703	0.69466	0.22953	$2.5^{+0.3}_{-0.3}$	$2.19^{+0.31}_{-0.24}$	4604010911	NICER
59500.64	3647	1.16781	0.35207	$2.9^{+0.3}_{-0.3}$	$2.47^{+0.41}_{-0.28}$	4604010912	NICER
59501.35	10186	0.91645	0.23872	$2.9^{+0.2}_{-0.2}$	$2.13^{+0.31}_{-0.22}$	4604010913	NICER
59502.49	7885	0.90298	0.23229	$2.7^{+0.3}_{-0.3}$	$1.96^{+0.24}_{-0.18}$	4604010914	NICER
59503.48	7906	1.08753	0.24026	$2.9^{+0.2}_{-0.2}$	$2.48^{+0.34}_{-0.24}$	4604010915	NICER
59504.51	4370	0.94073	0.18709	$2.8^{+0.3}_{-0.3}$	$2.23^{+0.35}_{-0.24}$	4604010916	NICER
59505.52	3600	1.07750	0.28458	$2.7^{+0.3}_{-0.3}$	$2.36^{+0.35}_{-0.25}$	4604010917	NICER
59506.22	826	1.14407	0.25471	$2.8^{+0.3}_{-0.3}$	$2.41^{+0.40}_{-0.29}$	4604010918	NICER
59508.15	553	0.95841	0.35484	$3.3^{+0.5}_{-0.5}$	$1.95^{+0.60}_{-0.39}$	4604010920	NICER
59510.21	3079	0.90257	0.14294	$2.8^{+0.3}_{-0.3}$	$2.31^{+0.38}_{-0.26}$	4604010921	NICER
59510.83	2777	0.03421	0.00044	$2.3^{+0.3}_{-0.3}$	$1.71^{+0.51}_{-0.39}$	00014135017	*Swift*
59511.91	2492	0.79374	0.14859	$2.9^{+0.3}_{-0.3}$	$1.91^{+0.27}_{-0.20}$	4604010922	NICER
59517.60	2745	0.22077	0.19720	3.0	< 0.15	4604011001	NICER
59520.47	3000	0.31967	0.30448	3.0	< 0.22	4604011002	NICER
59523.54	1200	0.27083	0.31064	3.0	< 0.27	4604011003	NICER
59524.53	1371	0.00000	0.00011	3.0	< 1.50	00014135018	*Swift*
59526.63	936	0.24679	0.31657	3.0	< 0.29	4604011004	NICER
59527.63	3924	0.00000	0.00005	3.0	< 0.24	00014135019	*Swift*
59529.83	636	0.24528	0.28465	3.0	< 0.30	4604011005	NICER
59529.87	1402	0.00000	0.00004	3.0	< 0.69	00014135021	*Swift*
59532.54	1143	0.25984	0.34356	3.0	< 0.29	4604011006	NICER
59535.32	1817	0.33352	0.37695	3.0	< 0.28	4604011007	NICER
59538.23	2041	0.20137	0.22903	3.0	< 0.19	4604011008	NICER
59541.33	1884	0.16030	0.14718	3.0	< 0.14	4604011009	NICER
59543.75	1996	0.00000	0.00009	3.0	< 0.39	00014135022	*Swift*

Table C.2. continued.

MJD	T_{exp} (s)	CR_{total} (cts s^{-1})	CR_{bkg} (cts s^{-1})	T_{in}/Γ (eV/-)	$f_{X,soft}$ 10^{-12} erg cm^{-2} s^{-1}	ObsID	Instrument
59557.41	2372	0.00042	0.00010	3.0	< 0.41	00014135023	*Swift*
59566.74	614	0.00000	0.00004	3.0	< 1.60	00014135025	*Swift*
59572.58	193	0.00000	0.00049	3.0	< 3.60	00014135024	*Swift*
59572.58	2635	0.00076	0.00034	3.0	< 0.38	00014135026	*Swift*
59584.90	2886	0.00000	0.00006	3.0	< 0.39	00014135027	*Swift*
59601.40	530	0.55849	0.40031	3.0	< 0.40	4595020114	NICER
59602.56	3203	0.33406	0.38072	3.0	< 0.26	4595020115	NICER
59603.21	1953	0.36457	0.39628	3.0	< 0.29	4595020116	NICER
59605.47	456	0.32456	0.28567	3.0	< 0.35	4595020118	NICER
59607.27	916	0.25218	0.26658	3.0	< 0.26	4595020119	NICER
59608.60	3275	0.25893	0.26392	3.0	< 0.20	4595020120	NICER
59609.72	1664	0.25661	0.24056	3.0	< 0.21	4595020121	NICER
59610.47	2922	0.21253	0.17810	3.0	< 0.15	4595020122	NICER
59611.79	997	0.17352	0.16539	3.0	< 0.18	4595020123	NICER
59612.47	1252	0.19968	0.18684	3.0	< 0.18	4595020124	NICER
59613.37	1469	0.29340	0.25956	3.0	< 0.22	4595020125	NICER
59619.34	859	0.27125	0.13602	$3.5^{+0.8}_{-0.8}$	$0.48^{+0.25}_{-0.15}$	4595020126	NICER
59619.40	872	0.23969	0.13188	$4.4^{+1.3}_{-1.0}$	$0.57^{+0.49}_{-0.23}$	4595020126	NICER
59619.72	905	0.25535	0.12572	$4.6^{+1.1}_{-0.9}$	$0.77^{+0.61}_{-0.30}$	4595020126	NICER
59625.99	787	0.42948	0.19563	$3.4^{+0.7}_{-0.6}$	$0.77^{+0.30}_{-0.19}$	4595020127	NICER
59626.06	1560	0.40192	0.18540	$3.7^{+0.5}_{-0.5}$	$0.81^{+0.27}_{-0.18}$	4595020128	NICER
59633.19	3138	0.56724	0.26562	$3.6^{+0.4}_{-0.4}$	$1.21^{+0.35}_{-0.23}$	4595020129	NICER
59635.13	10129	0.00938	0.00033	$3.2^{+0.3}_{-0.3}$	$0.77^{+0.27}_{-0.20}$	00014135999	*Swift*
59639.90	149	0.69128	0.11484	$2.3^{+0.9}_{-0.9}$	$1.68^{+0.51}_{-0.36}$	4604010104	NICER
59640.10	3423	0.76833	0.22940	$3.2^{+0.3}_{-0.3}$	$1.84^{+0.38}_{-0.26}$	4604010105	NICER
59642.13	3267	0.78206	0.27016	$3.2^{+0.3}_{-0.3}$	$1.75^{+0.36}_{-0.24}$	4604010106	NICER
59643.68	2485	0.02173	0.00044	$3.2^{+0.5}_{-0.5}$	$1.78^{+0.88}_{-0.58}$	00014135033	*Swift*
59645.48	2460	0.67195	0.18330	$3.2^{+0.3}_{-0.3}$	$1.71^{+0.38}_{-0.26}$	4604010107	NICER
59648.20	1991	0.59769	0.16090	$3.2^{+0.4}_{-0.4}$	$1.54^{+0.36}_{-0.24}$	4604010108	NICER
59650.19	2977	0.01445	0.00032	$3.2^{+0.5}_{-0.5}$	$1.58^{+0.88}_{-0.56}$	00014135034	*Swift*
59651.90	668	0.95060	0.47320	$2.6^{+0.6}_{-0.6}$	$1.39^{+0.35}_{-0.24}$	4604010109	NICER
59652.06	720	0.87778	0.38022	$3.6^{+0.6}_{-0.5}$	$2.12^{+0.91}_{-0.52}$	4604010110	NICER
59654.83	1787	0.68942	0.27128	$3.7^{+0.4}_{-0.4}$	$1.83^{+0.59}_{-0.37}$	4604010111	NICER
59656.16	2665	0.02177	0.00106	$3.0^{+0.4}_{-0.4}$	$1.48^{+0.68}_{-0.47}$	00014135036	*Swift*
59657.15	18390	0.55037	0.01046	—	$2.44^{+0.24}_{-0.21}$	0891801101	*XMM-Newton*
59663.82	3172	0.02176	0.00032	$2.8^{+0.4}_{-0.4}$	$1.52^{+0.58}_{-0.42}$	00014135037	*Swift*
59670.56	3127	0.02303	0.00049	$2.5^{+0.4}_{-0.4}$	$1.22^{+0.44}_{-0.32}$	00014135038	*Swift*
59678.08	4305	0.01115	0.00032	$2.8^{+0.5}_{-0.4}$	$0.68^{+0.34}_{-0.22}$	00014135039	*Swift*
59684.37	2922	0.01643	0.00087	$2.6^{+0.5}_{-0.5}$	$0.88^{+0.44}_{-0.29}$	00014135040	*Swift*
59691.98	6391	0.01377	0.00041	$3.1^{+0.4}_{-0.3}$	$1.08^{+0.39}_{-0.28}$	00014135041	*Swift*
59698.54	2627	0.01218	0.00135	$3.5^{+0.8}_{-0.8}$	$1.18^{+1.06}_{-0.56}$	00014135042	*Swift*
59705.30	3014	0.00199	0.00033	$3.0^{+0.0}_{-0.0}$	$0.12^{+0.13}_{-0.08}$	00014135043	*Swift*